

ADJOINT FOR ADVECTION SCHEMES ON THE SPHERE IN ICON MODEL

RAMAZ BOTCHORISHVILI

Faculty of Exact and Natural Sciences, Ivane Javakhishvili Tbilisi State University, Tbilisi, Georgia

HENDRIK ELBERN

Rhenish Institute for Environmental Research, University of Cologne, Cologne, Germany; Institute of Energy and Climate research 8: Troposphere, Research Center Jülich, Jülich, Germany

TAMARI JANELIDZE

Faculty of Exact and Natural Sciences, Ivane Javakhishvili Tbilisi State University, Tbilisi, Georgia; Institute of Energy and Climate research 8: Troposphere, Research Center Jülich, Jülich, Germany

ABSTRACT. Among the most advanced and sophisticated methods for state analysis of an atmospheric system is the four dimensional variational data assimilation. The numerically challenging task of this approach is the development and application of the adjoint model components. For tracer transport in fluid dynamics accuracy of numerical advection schemes is vital. It is even more important for applications in space-time variational data assimilation with adjoint model version. We propose novel straightforward and efficient approach - artificial source term method - for adjoint advection solver development. It has several benefits compared to traditional adjoint model building technique. One of the attractive features of the new approach is that it reuses existing advection solver code, thus resulting into significant reduction of time needed for adjoint solver development. The stability, accuracy and convergence of the adjoint schemes are investigated. The method is implemented and evaluated for the linear advection equation on the sphere in the Icosahedral Nonhydrostatic Model (ICON). Adjoint solvers developed by the conventional and the methods are compared against each other on a collection of standard advection test cases and variational data assimilation test cases developed here. The advantages of the artificial source term method is especially obvious in case of monotonic advection equation solvers, granting, e.g. absence of oscillations and nonphysical negative concentrations.

1. INTRODUCTION

Chemistry transport models (CTM) are widely used for air pollution modelling. These models are complex and they are usually solved numerically using operator splitting methods when equations describing chemical reactions, horizontal advection and vertical advection are treated separately at different splitting steps, see e.g. [1]. Incorporating observations from both in situ and remote sensing devices in CTMs, e.g. satellites etc., is essential for the quality of air pollution forecast. The method used for this purpose is called data assimilation that first appeared in meteorology [12]. Four dimensional variational data assimilation integrates

E-mail addresses: ramaz.botchorishvili@tsu.ge (Corresponding author), h.elbern@fz-juelich.de, t.janelidze@fz-juelich.de.

Date: June 19, 2018.

2010 Mathematics Subject Classification. 65M32, 65M08, 65Z99.

Key words and phrases. adjoint solver, linear advection equation, ICON model, variational data assimilation, inverse modeling.

into the model observational data distributed in space and finite time interval. For achieving this goal a constrained minimization problem is formulated where governing equations serve as constraints and a quadratic cost function measures misfits between observations and model forecast. Solving this minimization problem results in optimal initial data that are consistent with observations and with model dynamics. These data are used for improved forecasting on longer time interval, see [24], [3], [30], [22] for detailed exposition on the subject, see section 2 for the formulation of variational problem for the linear advection equation.

A central module in CTMs as part of a 4D-var system is the advection algorithm and its adjoint. [27] studied the influence of linear and non-linear numerical advection algorithm properties on variational data assimilation results in a 2D idealized scalar advection framework. Results suggested that exact the same scalar advection algorithm in forward and adjoint computations obtains, at lower cost, an optimal solution accuracy that is consistent with the forward model accuracy.

[25] investigated the impact of switches in non-oscillatory advection schemes for their adjoints. They showed that there is no possibility of smoothing the switches in nonoscillatory advection schemes to remove the discontinuities while retaining an obvious and desirable scaling property. On the basis of established equivalence between Eulerian backtracking or retro-transport and adjoint transport with respect to an air-mass-weighted scalar product, [10] studied the question which arises as to whether it is preferable to use the exact numerical adjoint, or the retro-transport model for a model that is not time-symmetric. They concluded that the presence of slope limiters in the Van Leer advection scheme can produce in sonic circumstances unrealistic, even negative adjoint sensitivities. The retro-transport equation, on the other hand, generally produces robust and realistic results.

In the context of the GEOS-Chem [8] tested the accuracy of the adjoint model by comparing adjoint to finite difference sensitivities, which are shown to agree within acceptable tolerances. They explore the robustness of these results, noting how discontinuities in the advection routine hinder, but do not entirely preclude, the use of such comparisons for validation of the adjoint model.

A comprehensive study on the consistency of the discrete adjoints of upwind numerical schemes was provided by [14]. Both linear and nonlinear discretizations of the one-dimensional advection equation are considered, representing finite differences or finite volumes and slope or flux-limited techniques, respectively. [4] studied the effect of using discrete and continuous adjoints of the advection equation in chemical transport modeling numerically. They concluded that discrete advection adjoints are more accurate in point-to-point comparisons against finite differences, whereas the continuous adjoints of advection perform better as gradients for optimization in 4D-Var data assimilation.

Considering a variational implementation of the RETRO-TOM model, [5] demonstrated a time symmetric forward advection scheme with second-order moments to be efficiently exploited in the backward adjoint calculations, at least for problems in which flux limiters in the advection scheme are not required. For this case the authors found the flexibility and stability of a 'finite difference of adjoint' formulation with the accuracy of an 'adjoint of finite difference' formulation.

[9] examined the tangent linear and adjoint versions of NASA's Goddard Earth Observing System version 5 (GEOS-5). Tests exhibited that piecewise parabolic methods with flux limiters development of unrealistically large perturbations within the tangent linear and adjoint models, and that using a linear third-order scheme for the linearised model produces better behaviour.

Iterative methods are used for minimizing the quadratic cost function. Quasi-Newton limited memory methods are among most popular minimization algorithms [13]. A numerically challenging task in variational data assimilation is the development of the adjoint model for the gradient computation that is used by quasi Newton algorithm. For the linear advection equation, as demonstrated in [26], the results depend on the implementation of adjoint advection schemes especially in case of nonlinear schemes. Several different approaches can be used for adjoint solver development, see e.g. [12], [19] for derivation of adjoint equations in continuous setting for which numerical solver has to be developed, see e.g. [25]() for the development of adjoint in discrete setting - i.e. adjoint of a given numerical advection scheme, and see [7] for the development of adjoint code based on powerful automated differentiation tool Tapenade.

Here we propose simple and powerful approach for the adjoint development for linear advection equation in conservative form. Our approach is based on introducing artificial source term that ensures consistency

of the adjoint numerical scheme with the adjoint of the linear advection equation under consideration. Implementation of our approach is easy and time efficient: it essentially reuses given linear advection solvers with minor modifications, maintains accuracy and stability of the given parent solver and it uses the same parallelization routines. The proposed method is general, though here we consider advection schemes on triangular mesh of the sphere in the ICON model. See subsection 3.1 for short description and [29] for details, as part of broader effort on development of a next generation 4D-Var data assimilation system with CTM.

The paper is organized as follows: in section 2 the linear advection equation on the sphere is given, the variational problem on data assimilation is formulated, and the adjoint and cost functions are given; in section 3 a new method for building adjoint scheme is proposed that is applied for building the adjoint solver using linear advection schemes in the ICON model, the properties of the developed adjoint schemes are investigated theoretically; in section 4 the new method is studied numerically on test problems in the context of data assimilation for tracer transport models.

2. VARIATIONAL PROBLEM FORMULATION FOR LINEAR ADVECTION

2.1. Linear advection equation on the sphere. The linear advection equation in conservative form writes:

$$(1) \quad \frac{\partial(\rho q)}{\partial t} + \nabla \cdot (\rho q \vec{v}) = 0,$$

where ρ and q are fluid density and mixing ratio, respectively. We are interested in their advection on the surface of the sphere Ω . Therefore $\vec{v} = (v_\lambda, v_\theta)^T$ is the 2D horizontal wind vector and $\nabla \cdot$ is a spherical horizontal divergence operator given by

$$(2) \quad \nabla \cdot v = \frac{1}{\sin \theta} \left[\frac{\partial v_\lambda}{\partial \lambda} + \frac{\partial (v_\theta \sin \theta)}{\partial \theta} \right],$$

with $0 \leq \lambda \leq 2\pi$ longitude and $0 \leq \theta \leq \pi$ latitude. For simplicity, we take the radius R of the sphere to be one.

Throughout this paper in (1) $\rho = \rho(t, \lambda, \theta) > 0$ and $v = v(t, \lambda, \theta)$ are sufficiently smooth given functions, $q = q(t, \lambda, \theta)$ is the unknown function that should be determined from the equation (1) subject to the initial condition that writes:

$$(3) \quad q(0, \lambda, \theta) = q_0(\lambda, \theta),$$

where $q_0(\lambda, \theta)$ is a sufficiently smooth given function.

Notice that initial condition (3) is given on the surface of the sphere. Because of this initial condition is sufficient and no boundary conditions are needed, the problem (1)-(3) is well posed for any finite time interval $[0, T]$.

2.2. Variational problem, adjoint equation, gradient of cost function. Consider the following cost function:

$$(4) \quad J(q_0) = f^b(q_0, q^b) + \int_0^T \int_\Omega f^o(q, q^o, t, \lambda, \theta) d\lambda d\theta dt,$$

where q_0 is initial value function from the initial condition (3); $q^b = q^b(\lambda, \theta)$ is given, it is the so called background function that is also used as first guess for iteration method minimizing $J(q_0)$ with respect to q_0 ; in q^o the superscript "o" stands for observations and is a given function; the functions f^b and f^o will be detailed in next subsection. Function f^b measures the misfit between initial and background functions, while f^o measures misfit between mixing ratio and observations. Here we assume f^b and f^o are smooth enough, we also assume that gradients of f^b and f^o with respect to q_0 , denoted here via $\nabla_{q_0} f^b$ and $\nabla_{q_0} f^o$ respectively, can be computed analytically.

Now we can state the variational data assimilation problem in the following way:

Problem 2.1 (Variational data assimilation). Find a initial function q_0 minimizing cost function (4) subject to constraints (1),(3).

The gradient of cost function $J(q_0)$ writes:

$$(5) \quad \nabla_{q_0} J(q_0) = \nabla_{q_0} f^b(q_0, q^b) - \rho(0, \lambda, \theta) q^*(0, \lambda, \theta),$$

where $q^*(0, \lambda, \theta)$ is solution at $t = 0$ of the following adjoint equation

$$(6) \quad \rho \left(\frac{\partial q^*}{\partial t} + v \cdot \nabla q^* \right) = \nabla_q f^o(q, q^o, t, \lambda, \theta),$$

which is subject to the initial condition at $t = T$, in particular,

$$(7) \quad q^*(T, \lambda, \theta) = 0.$$

Notice that in the adjoint equation (6) on the right hand side the function q is the solution of the conservative linear advection equation (1) with initial condition (3). Notice also that the problem (1),(3) is integrated forward in time and the problem (6),(7) is integrated backward in time. Because of this reason the problem (1),(3) is often referred as forward problem and the problem (6), (7) is referred as adjoint problem. The same applies to the numerical solvers, i.e. forward solver and adjoint solver. Using these terms we can easily formulate procedure for the gradient computation. In particular, we have:

Procedure 2.1 (Computing the gradient of the cost function).

- (1) Solve the forward problem (1),(3) and store $q(t, \lambda, \theta)$.
- (2) Put $q(t, \lambda, \theta)$ on the right hand side of the equation (6) and solve the adjoint problem (6), (7), store $q^*(0, \lambda, \theta)$.
- (3) Insert $q^*(0, \lambda, \theta)$ in (5) and compute the gradient of the cost function $J(q_0)$ defined by (4).

2.3. Cost function. Cost functions of variational data assimilation problem are mainly given in discrete or semi-discrete form in scientific literature, see e.g. [1, 22, 30] for fully discrete cost functions and see [2, 3, 30] for semi-discrete cost functions. Under semi-discrete version we mean cost function where continuous time integration is used. Here we establish a relationship between discrete, semi-discrete and continuous cost functions that is needed later for studying convergence of developed numerical schemes. For this purpose we have to make a discretization in space and time of dependent and independent variables. Since finite volume schemes are of interest of the present paper, we denote by Ω_j finite volume cell j , $\Omega_j \subset \Omega$, $\cup_{j=1}^{N_c} \Omega_j = \Omega$, where $|\Omega_j|$ is area of the cell Ω_j , and N_c is number of cells. The average value of function q on Ω_j at time t is denoted as $q_j(t)$. The same value at time $t = t_n$ is denoted as q_j^n , $t_n = n\Delta t$, $n = 0, 1, \dots, N_T$, where $\Delta t = T/N_T$ is time discretization step, and N_T is number of nodal points in time. In the data assimilation context all discretized function values at time t are interpreted as vectors, e.g. $\vec{q}(t) = (q_1(t), q_2(t), \dots, q_{N_c}(t))^T$, $\vec{q}^n = (q_1^n, q_2^n, \dots, q_{N_c}^n)^T$, since such notations are convenient for formulating cost function. Adopting our notations the semidiscrete cost function from [2] writes:

$$(8) \quad J(\vec{q}_0) = \frac{1}{2} (\vec{q}^b - \vec{q}_0)^T B^{-1} (\vec{q}^b - \vec{q}_0) + \frac{1}{2} \int_{t_0}^{t_{N_T}} (\vec{q}^o(t) - H[\vec{q}(t)])^T R^{-1} (\vec{q}^o(t) - H[\vec{q}(t)]) dt,$$

where B and R matrices are the background and observation error covariance matrices, respectively, $\vec{q}^o(t) = (q_{i_1}^o(t), q_{i_2}^o(t), \dots, q_{i_{N_o}}^o(t))^T$, $1 \leq i_k \leq N_c$, $k = 1, 2, \dots, N_o$, N_o is number of observations, $N_o < N_c$. Operator H projects the model state to observation space that practically means the following: $H[\vec{q}(t)] = (q_{i_1}(t), q_{i_2}(t), \dots, q_{i_{N_o}}(t))^T$. We denote by \mathcal{O} the set of indices corresponding to observations, $\mathcal{O} = \{i_1, i_2, \dots, i_{N_o}\}$.

The fully discrete version of the cost function from [1] writes:

$$(9) \quad J(\vec{q}_0) = \frac{1}{2} [\vec{q}^b - \vec{q}_0]^T B^{-1} [\vec{q}^b - \vec{q}_0] + \frac{1}{2} \sum_{n=0}^{N_T} [\vec{q}^{on} - H(\vec{q}^n)]^T R^{-1} [\vec{q}^{on} - H(\vec{q}^n)].$$

If we assume that covariance matrices B and R are the same in (8) and (9) then for the compatibility of semi-discrete and discrete cost functions the following modification is necessary:

$$(10) \quad J(\vec{q}_0) = \frac{1}{2}[\vec{q}^b - \vec{q}_0]^T B^{-1}[\vec{q}^b - \vec{q}_0] + \frac{T}{2N_T} \sum_{n=0}^{N_T} [\vec{q}^{on} - H(\vec{q}^n)]^T R^{-1}[\vec{q}^{on} - H(\vec{q}^n)],$$

Notice that (8) and (10) are compatible in the sense that when $N_T \rightarrow \infty$ limit of discrete cost function (10) coincides with semidiscrete cost function (8).

Studying covariance matrices is out of scope of this paper. Therefore, without loss of generality and for the convenience of further exposition, we replace inverse covariance matrices by some positive definite kernels denoted by $K_b(\xi, \xi')$ and $K_o(\xi, \xi')$, $\xi, \xi' \in \Omega$, $\xi = (\lambda, \theta)$, $\xi' = (\lambda', \theta')$, and we define the function f^b from (4) in the following way:

$$(11) \quad f^b(q_0, q^b) = \frac{1}{2|\Omega|^2} \int_{\Omega} \int_{\Omega} K_b(\xi, \xi')[q_0(\xi) - q^b(\xi)][q_0(\xi') - q^b(\xi')] d\xi d\xi'.$$

After standard discretization of (11) we have:

$$(12) \quad J^b = \sum_{i=1}^{N_c} \sum_{j=1}^{N_c} \frac{|\Omega_i||\Omega_j|}{2|\Omega|^2} K_b(\xi_i, \xi'_j)[q_{0j} - q_i^b][q_{0j} - q_j^b] = \frac{1}{2}[\vec{q}^b - \vec{q}_0]^T K^b[\vec{q}^b - \vec{q}_0],$$

where K^b is a symmetric positive definite matrix with elements

$$K_{ij}^b = \frac{|\Omega_i||\Omega_j|}{2|\Omega|^2} K_b(\xi_i, \xi'_j), \quad i, j = 1, 2, \dots, N_c.$$

Thus consistency is ensured between discrete and continuous versions of background terms (11) and (12), i.e. $\lim_{N_c \rightarrow \infty} J^b = f^b$. The formulation will allow us to study the impact of mesh refinement on data assimilation in section 4.

By analogy with (12) we define J^o and its continuous version:

$$(13) \quad J^o = \frac{T}{2N_T} \sum_{n=0}^{N_T} \sum_{i \in \mathcal{O}} \sum_{j \in \mathcal{O}} \frac{|\Omega_i||\Omega_j|}{2|\Omega^o|^2} K_o(\xi_i, \xi'_j)[q_i^{on} - q_j^{on}][q_j^{on} - q_j^n] = \frac{T}{2N_T} \sum_{n=0}^{N_T} [\vec{q}^{on} - H(\vec{q}^n)]^T K^o[\vec{q}^{on} - H(\vec{q}^n)],$$

$$(14) \quad f^o(q, q^o, t, \xi) = \begin{cases} \frac{[q(t, \xi) - q^o(t, \xi)]}{2|\Omega^o|^2} \int_{\Omega^o} K_o(\xi, \xi')[q(t, \xi') - q^o(t, \xi')] d\xi', & \xi \in \Omega^o, \\ 0, & \text{otherwise,} \end{cases}$$

where

$$K_{ij}^o = \frac{|\Omega_i||\Omega_j|}{2|\Omega^o|^2} K_o(\xi_i, \xi'_j), \quad i, j \in \mathcal{O}, \quad \Omega^o = \cup_{i \in \mathcal{O}} \Omega_i.$$

Consequently we have

$$(15) \quad \nabla_q f^o(q, q^o, t, \xi) = \begin{cases} \frac{1}{|\Omega^o|^2} \int_{\Omega^o} K_o(\xi, \xi')[q(t, \xi') - q^o(t, \xi')] d\xi', & \xi \in \Omega^o, \\ 0, & \text{otherwise.} \end{cases}$$

Notice that in (14) we assume that observations are given on a subdomain Ω^o , $|\Omega^o| > 0$.

3. NUMERICAL SCHEMES

3.1. ICON grids. The name "ICON" stands for the joint project of the Max Plank Institute for Meteorology (MPI-M) and the German Weather Service (DWD) on development of **IC**Osahedral **N**onhydrostatic models [29]. In the earlier version of ICON model triangular and hexagonal discretizations were tested and later only the triangular version of the icosahedral mesh is used [29]. In this paper we use the triangular version of icosahedral grids from "Published list of DWD (EDZW) ICON grids" by MPI-M and DWD given at <http://icon-downloads.zmaw.de/>. Meshes are referred as " $Rn_r Bn_b$ grids" and from this name one can recover the algorithm how the grid was constructed. In particular, starting point in any " $Rn_r Bn_b$ grid" is

an icosahedron with vertices on the sphere that is entirely projected onto the sphere, then edges along a great arc are divided in n_r equal parts and then each edge of the obtained triangles are recursively divided n_b times. See [21, 29] for detailed description of the algorithm, for different optimization approaches and for grid characteristics. Some important characteristics of these meshes are given in the Table 1 in [29] that shows non uniformity of Rn_rBn_b grids in terms of triangle area ratios that can reach values as high as 1.53 for $R2B7$ grid. The same table also shows that the ratio is increasing together with mesh refinement. Here we also give some additional characteristics of Rn_rBn_b grids in the Table 1. When grids are refined the edge ratio is also increasing and its maximum can reach 1.34 for $R2B7$ grid. Though inside each triangle the edge ratio is almost constant and it increases very slowly, for example in particular, from 1.1734 for $R2B2$ grid to 1.1761 for $R2B7$ grid. Close to 1 edge ratio also means that triangular mesh changes smoothly on the surface of the sphere. $R2B7$ is the finest grid we consider in this paper since. Notice that our cost function accounts for the variability of grid.

Table 1 ICON grids, $R2Bn_b$

Grid	Number of triangular cells	Number of triangle edges	Min triangle cell area, km ²	Max:min edge length ratio, global	Max:min edge length ratio, triangle	Min edge length, km
R2B0	80	120	6010381.55	1.14	1.1350	3526.95
R2B1	320	480	1440873.32	1.17	1.1660	1737.06
R2B2	1280	1920	333434.84	1.21	1.1734	836.96
R2B3	5120	7680	78835.01	1.24	1.1750	407.12
R2B4	20480	30720	18777.28	1.27	1.1754	198.71
R2B5	81920	122880	4507.50	1.30	1.1755	97.36
R2B6	327680	491520	1089.56	1.32	1.1756	47.87
R2B7	1310720	1966080	265.08	1.34	1.1761	23.61

3.2. Linear advection schemes in ICON model. Tracer transport schemes in the ICON triangular version are based on [15] for finite volume discretization and on [20] for high order reconstruction, both methods adapted to triangular grids on a sphere. The scheme is referred as ICON-FFSL (ICON-Flux Form Semi-Lagrangian) in [11] for its second order version. In this paper we will also use the same abbreviation for ICON tracer transport schemes. These schemes can be used with or without limiters. Here we build adjoint schemes for both cases. Adjoint without limiter is given in the section 3.3 and the adjoint with limiter is introduced in the section 3.4. Limiters in ICON-FFSL schemes are based on Zalesak's **F**lux **C**orrected **T**ransport (FCT) by [32] the limiter and its positive definite modifications by [23] and [6]. Details including numerical results on ICON tracer transport schemes are given in <http://www.cgd.ucar.edu/cms/pel/transport-workshop/2011/16-Reinert.pdf>, [29] and [11]. For the convenience of further exposition on constructing adjoint schemes the above finite volume advection schemes ICON-FFSL can be written in the following flux form:

$$(16) \quad \frac{\rho_j^{n+1} q_j^{n+1} - \rho_j^n q_j^n}{\Delta t} + \frac{1}{|\Omega_j|} \sum_{i \in I_j} F_{ji}(\{\bar{\rho}_k^n, \bar{v}_k^n, q_k^n\}_{k \in K_{ji}}, \vec{n}_{ji}, l_{ji}) = 0,$$

where I_j is a set of reference numbers to cell interfaces surrounding cell Ω_j , i.e. I_j consists of three elements in case of triangular cell. F_{ji} is a numerical flux function on the cell interface between cells Ω_j and Ω_i , set K_{ji} contains reference numbers to cells that are used for computing the numerical flux function F_{ji} , \vec{n}_{ji} is a unit outward normal of the cell interface, l_{ji} is length of the edge shared by triangles j and i , $\bar{\rho}_k^n$ and \bar{v}_k^n stands for time average of ρ_k and \vec{v}_k on $[[t_n, t_{n+1}]$. Notice that $K_{ji} = K_{ij}$, $l_{ji} = l_{ij}$, $\vec{n}_{ji} = -\vec{n}_{ij}$, $F_{ji} = -F_{ij}$. The latter ensures mass conservation of the scheme (16).

3.3. Integration by parts method for adjoint schemes. Here we consider adjoint scheme for ICON-FFSL with numerical flux function without limiters. In this case ICON-FFSL scheme (16) can be equivalently written in the following form:

$$(17) \quad \frac{\rho_j^{n+1} q_j^{n+1} - \rho_j^n q_j^n}{\Delta t} + \frac{1}{|\Omega_j|} \sum_{i \in S_j} \alpha_{ji}(\{\bar{\rho}_k^n, \bar{v}_k^n\}_{k \in K_{ji}}) q_i^n = 0, \quad S_j = \cup_{i \in I_j} K_{ji},$$

where S_j contains a reference number to cells on the stencil of the scheme, see Fig. 20. The scheme (17) is linear with respect to \bar{q}^n and it is the starting point for building the adjoint, i.e. for deriving the scheme that is consistent with equation (6). In the latter equation the approximation of the time derivative and the right hand side is straightforward. The spatial derivatives can be approximated, e.g. by means of rewriting second term in (17) in matrix form and then using transpose matrix. Equivalent but easy to use approach is using discrete analogue of integration by parts formula, i.e. discrete analogue of the approach which was used for the derivation of (6). For the convenience of further exposition we set: $\alpha_{ji} = 0$, if $i \notin S_j$. Thus we have

$$(18) \quad \sum_j |\Omega_j| q_j^{*,n} \frac{1}{|\Omega_j|} \sum_{i \in S_j} \alpha_{ji}(\{\bar{\rho}_k^n, \bar{v}_k^n\}_{k \in K_{ji}}) q_i^n = \sum_j \sum_i \alpha_{ji}(\{\bar{\rho}_k^n, \bar{v}_k^n\}_{k \in K_{ji}}) q_i^n q_j^{*,n} = \\ \sum_i \sum_j \alpha_{ji}(\{\bar{\rho}_k^n, \bar{v}_k^n\}_{k \in K_{ji}}) q_i^n q_j^{*,n} = \sum_i |\Omega_i| q_i^n \frac{1}{|\Omega_i|} \sum_{j \in S_i^*} \alpha_{ji}(\{\bar{\rho}_k^n, \bar{v}_k^n\}_{k \in K_{ji}}) q_i^{*,n},$$

where S_i^* is set of indexes for which $\alpha_{ji} \neq 0$. On account of (18), (17) and (6) adjoint numerical scheme writes:

$$(19) \quad \bar{\rho}_j^n \frac{q_j^{*,n+1} - q_j^{*,n}}{\Delta t} + \frac{1}{|\Omega_j|} \sum_{i \in S_j^*} \alpha_{ji}(\{\bar{\rho}_k^n, \bar{v}_k^n\}_{k \in K_{ji}}) q_i^{*,n} = \nabla_q f^o(q_j^{*,n}, q_j^{o,n}, t_n, \xi_j).$$

Coefficients α_{ji} are given in the appendix 6.4.

3.4. Artificial source term method for adjoint schemes. In this section we introduce a simple and efficient new method for developing the adjoint scheme and we apply it for building the adjoint based on ICON-FFSL. The method can be used when the numerical flux function is limited with or without flux limiters. Our starting point is ICON-FFSL in flux form (16). Assuming the scheme is consistent with equation (1) the goal is constructing a numerical scheme that is consistent with the equation (6). The latter can be equivalently written

$$(20) \quad \rho \frac{\partial q^*}{\partial t} + \nabla \cdot (\rho q^* \vec{v}) = q^* \nabla \cdot (\rho \vec{v}) + \nabla_q f^o(q, q^o, t, \xi),$$

where $\nabla_q f^o(q, q^o, t, \xi)$ is defined by (15). We will use this equivalent formulation of the adjoint equation as starting point of our method. The equation in the form (20) is a good choice because we can effortlessly reuse discretization schemes developed for the linear advection equation in conservative form (1). In particular, the spatial discretization of ICON-FFSL (16) can be reused for the second and first term respectively, both in the left hand side and in the right hand side of the equation (20). As a result we have the following numerical scheme for the gradient computation

$$(21) \quad \bar{\rho}_j^n \frac{q_j^{*,n+1} - q_j^{*,n}}{\Delta t} + \frac{1}{|\Omega_j|} \sum_{i \in I_j} F_{ji}(\{\bar{\rho}_j^n, \bar{v}_k^n, q_k^{*,n}\}_{k \in K_{ji}}, \vec{n}_{ji}, l_{ji}) = \\ \frac{1}{|\Omega_j|} \sum_{i \in I_j} F_{ji}(\{\bar{\rho}_j^n, \bar{v}_k^n, q_j^{*,n}\}_{k \in K_{ji}}, \vec{n}_{ji}, l_{ji}) + \nabla_q f^o(q_j^n, q_j^{o,n}, t_n, \xi_j).$$

Notice that the first sum in the numerical scheme (21) is exactly the same as the sum in (16). The second sum in (21) is in principle the same with $q_j^{*,n}$ instead of $q_k^{*,n}$ that makes the computation of the sum even

easier. Therefore the particularly interesting feature of the numerical scheme (21) is the following: it makes easy reusing of the source code of the parent scheme, in our case ICON-FFSL scheme, and that dramatically reduces time needed for adjoint code development, e.g. it took just a couple of days in our case.

3.5. Properties of the adjoint scheme with artificial source term. It is expected that the adjoint scheme constructed by artificial source term method will have good properties in the case if the parent scheme has the same good properties as well. According to Lax's equivalence theorem the minimal set of properties of the schemes ensuring convergence are consistency and stability. Therefore we will assume that parent scheme has these properties and then we prove that its descendant adjoint scheme also enjoys the same properties.

Theorem 3.1 (Consistency theorem). Suppose q, ρ, \vec{v}, q^* are sufficiently smooth and numerical scheme (16) is consistent with the linear advection equation (1) in the sense of local truncation error. Then adjoint scheme with artificial source term (21) is also consistent with adjoint equation (20).

Proof. From the consistency requirement of numerical scheme (16) with equation (1) we easily obtain consistency between corresponding terms in the scheme and equation. In particular it is clear that the expression

$$(22) \quad \frac{\rho_j^{n+1} q_j^{n+1} - \rho_j^n q_j^n}{\Delta t} \text{ is consistent with } \frac{\partial(\rho q)}{\partial t}$$

at (t_n, ξ_j) and therefore the expression

$$(23) \quad \frac{1}{|\Omega_j|} \sum_{i \in I_j} F_{ji}(\{\bar{\rho}_k^n, \bar{v}_k^n, q_k^n\}_{k \in K_{ji}}, \vec{n}_{ji}, l_{ji}) \text{ is consistent with } \nabla \cdot (\rho q \vec{v}).$$

at (t_n, ξ_j) . Assuming in the above expression $q_k = q_j$ means that q is constant on the stencil and therefore

$$(24) \quad \frac{1}{|\Omega_j|} \sum_{i \in I_j} F_{ji}(\{\bar{\rho}_k^n, \bar{v}_k^n, q_j^n\}_{k \in K_{ji}}, \vec{n}_{ji}, l_{ji}) \text{ is consistent with } q_j \nabla \cdot (\rho \vec{v}).$$

Similarly with (22) it is evident that the first and fourth term in the numerical scheme with artificial source term (21) are consistent at (t_n, ξ_j) with first and fourth term in the adjoint equation (20). Substituting q_j^n with q_j^{*n} in (23) and (24) yields consistency at (t_n, ξ_j) of the second and third terms in the numerical scheme (21) with the second and third term in the equation (20) that concludes the proof. \square

Theorem 3.2 (Stability theorem). Suppose

- (1) ρ is time independent.
- (2) $\rho \geq \rho_{min} > 0$.
- (3) $\rho, \vec{v}, F, q, \tilde{q}$ are smooth enough.
- (4) $\vec{q}^n, \tilde{\vec{q}}^n$ are numerical solutions constructed by numerical scheme (16) with initial values $\vec{q}_0, \tilde{\vec{q}}_0$ respectively.
- (5) Under Courant-Friedrichs-Levy (CFL) condition with CFL number CFL_0 the numerical scheme (16) is stable in some norm:

$$(25) \quad \|\vec{q}^{n+1} - \tilde{\vec{q}}^{n+1}\| \leq (1 + C_0 \Delta t) \|\vec{q}^n - \tilde{\vec{q}}^n\|, \quad 0 \leq n < N_t,$$

constant C_0 is independent of n .

If 1 – 5 are valid the numerical scheme with artificial source term (21) is also stable under CFL condition with CFL number $CFL_* = 2CFL_0$ in the same norm,

$$(26) \quad \|\vec{q}^{*,n} - \tilde{\vec{q}}^{*,n}\| \leq C_1 \|\vec{q}_0^* - \tilde{\vec{q}}_0^*\|, \quad 0 < n \leq N_t,$$

where C_1 is some constant independent of n .

Proof. Numerical scheme (21) equivalently writes:

$$(27) \quad \frac{1}{2} \bar{\rho}_j^n \frac{q_j^{*,1,n+1} - q_j^{*,n}}{\Delta t} + \frac{1}{|\Omega_j|} \sum_{i \in I_j} F_{ji}(\{\bar{\rho}_j^n, \bar{v}_k^n, q_k^{*,n}\}_{k \in K_{ji}}, \bar{n}_{ji}, l_{ji}) = 0,$$

$$\frac{1}{2} \bar{\rho}_j^n \frac{q_j^{*,2,n+1} - q_j^{*,n}}{\Delta t} = \frac{1}{|\Omega_j|} \sum_{i \in I_j} F_{ji}(\{\bar{\rho}_j^n, \bar{v}_k^n, q_k^{*,n}\}_{k \in K_{ji}}, \bar{n}_{ji}, l_{ji}) + \nabla_q f^o(q_j^n, q_j^{o,n}, t_n, \xi_j),$$

$$q_j^{*,n+1} = \frac{1}{2}(q_j^{*,1,n+1} + q_j^{*,2,n+1}).$$

The first numerical scheme in (27) can be obtained from (21) by replacing $\bar{\rho}_j^{n+1}$ with $\bar{\rho}_j^n$, see requirement 1 of the theorem, and by replacing Δt with $2\Delta t$. Therefore, similar to (25), the estimate is valid for $q^{*,1,n+1}$ under the CFL condition with CFL number CFL_* and we have:

$$(28) \quad \|\bar{q}^{*,1,n+1} - \vec{q}^{*,1,n+1}\| \leq (1 + 2C_0\Delta t) \|\bar{q}^{*,n} - \vec{q}^{*,n}\|, \quad 0 \leq n < N_t.$$

The first term in the right hand side of the second equation in (27) is consistent with $q_j \nabla \cdot (\rho \bar{v})$ according to theorem 3.1. Therefore, on account of the requirements of theorem 3.2, we can assume that there exists a constant C_2 independent of n such that the following inequality holds true:

$$(29) \quad \frac{2}{\bar{\rho}_j^n |\Omega_j|} \left| \sum_{i \in I_j} [F_{ji}(\{\bar{\rho}_j^n, \bar{v}_k^n, q_k^{*,n}\}_{k \in K_{ji}}, \bar{n}_{ji}, l_{ji}) - F_{ji}(\{\bar{\rho}_j^n, \bar{v}_k^n, \tilde{q}_k^{*,n}\}_{k \in K_{ji}}, \bar{n}_{ji}, l_{ji})] \right| \leq 2C_2 |q_j^{*,n} - \tilde{q}_j^{*,n}|.$$

The second term on the right hand side of the second equation in (27) does not depend on q^* . Therefore, by analogy with explicit Euler time integration scheme on account of (29) we obtain the following stability inequality:

$$(30) \quad \|\bar{q}^{*,2,n+1} - \vec{q}^{*,2,n+1}\| \leq (1 + 2C_2\Delta t) \|\bar{q}^{*,n} - \vec{q}^{*,n}\|, \quad 0 \leq n < N_t.$$

Putting together the third equation in (27), (26) and (30) we obtain the following stability estimate for q^* for one time step:

$$(31) \quad \|\bar{q}^{*,n+1} - \vec{q}^{*,n+1}\| \leq (1 + [C_0 + C_2]\Delta t) \|\bar{q}^{*,n} - \vec{q}^{*,n}\|, \quad 0 \leq n < N_t.$$

From (31) we arrive to (26) with $C_1 = \exp((C_0 + C_2)T)$ which concludes the proof. \square

Remark 3.1. $CFL_* = 2CFL_0$ is needed for the theoretical estimates only. In practice when calculating numerical tests the adjoint numerical scheme with artificial source term is stable under the same CFL condition as a parent scheme.

Remark 3.2. Theorem 3.2 deals with time independent ρ . The case with time dependent ρ can be also be easily treated by a different equivalent formulation of the adjoint scheme with artificial source term. In particular a numerical scheme of the form

$$\bar{\rho}_j^n \frac{q_j^{*,n+1} - q_j^{*,n}}{\Delta t} = RHS^n$$

can be equivalently written as the following two step scheme:

$$\frac{\bar{\rho}_j^{n+1} q_j^{*,1,n+1} - \bar{\rho}_j^n q_j^{*,n}}{\Delta t} = RHS^n, \quad \frac{q_j^{*,2,n+1} - q_j^{*,1,n+1}}{\Delta t} = \frac{1}{\bar{\rho}_j^n} \frac{\bar{\rho}_j^{n+1} - \bar{\rho}_j^n}{\Delta t} q_j^{*,2,n+1}.$$

The second scheme is an implicit Euler scheme and obtaining stability estimate is trivial. For obtaining stability estimate for the first scheme theorem 3.2 can be invoked by similar arguments.

Remark 3.3. Theorems 3.1 and 3.2 are sufficient for concluding convergence of artificial source term scheme since consistency and stability ensure convergence according to Lax equivalence theorem.

4. NUMERICAL TESTS

4.1. Input for tests. Here we consider two different types of tests: linear advection test cases and data assimilation test cases. Linear advection test cases are used for comparing adjoint schemes with their parent scheme. Therefore numerical calculations are done with three schemes: ICON-FFSL, adjoint scheme obtained by integration by parts formula, and an adjoint scheme by introducing artificial source term. Two different flux limiters are used together with ICON-FFSL and with the adjoint with artificial source term. In particular flux limiters from [32], [23] and from [32], [6] are used. Data assimilation test cases are used for comparing two adjoint schemes presented in this paper. In both test cases the true solution is compared with numerical solutions computed with the above mentioned numerical schemes. Errors in numerical solutions are measured in three different absolute and relative norms. In particular the following norms are used:

$$l_{1,rel} = \frac{\sum_{i=1}^{N_c} |\Omega_i| |q_i - q_i^{true}|}{\sum_{i=1}^{N_c} |\Omega_i| |q_i^{true}|}, \quad l_{1,abs} = \sum_{i=1}^{N_c} |q_i - q_i^{true}|,$$

$$l_{2,rel} = \frac{\sqrt{\sum_{i=1}^{N_c} |\Omega_i| (q_i - q_i^{true})^2}}{\sqrt{\sum_{i=1}^{N_c} |\Omega_i| (q_i^{true})^2}}, \quad l_{2,abs} = \sqrt{\sum_{i=1}^{N_c} (q_i - q_i^{true})^2},$$

$$l_{\infty,rel} = \frac{\max_{i=1, \dots, N_c} |q_i - q_i^{true}|}{\max_{i=1, \dots, N_c} |q_i^{true}|}, \quad l_{\infty,abs} = \max_{i=1, \dots, N_c} |q_i - q_i^{true}|.$$

Notice that l_1 and l_2 measure integral characteristics and l_∞ measures the maximum local deviation from the true solution, but none of them measures either oscillations in the numerical solution directly or shape preservation. Therefore where appropriate these two criteria will be also used. We also consider magnitude of cost function and norms of its gradient as most important criteria for evaluating performance of numerical schemes in case of data assimilation tests cases that are given in the subsection 4.3.

Standard test cases are available in scientific literature, such as [16], [17], [18], [31], [32]. We collected them in the appendix 6.1, in Table 2, and in Table 3 as collection of initial conditions and velocity fields. In particular we define five different initial scalar fields with references in Table 2 and four different velocity vector fields as given in Table 3. Combination of initial scalar fields and velocity vector fields are used for defining different test cases below.

4.2. Linear advection test cases.

4.2.1. ICON-FFSL, standard adjoint and adjoint with artificial source term. First we compare the parent scheme ICON-FFSL with two derived adjoint schemes presented in this paper. Notice that ICON-FFSL is consistent with equation (1) and adjoint schemes are consistent with equation (6). These two equations coincide with each other if $\rho = const$, $\nabla_q f^o = 0$ and $div \vec{v} = 0$. The latter condition is satisfied by wind fields 1,2 and 4 in the Table 3. We also set $\rho = 1$. With this selection of parameters we can compare all three numerical schemes against each other on solutions of the problem (1),(3). In particular we consider the following test problems

- Solid body rotation with cosine bell.
- Solid body rotation with slotted cylinder.
- Deformational flow with two cosine bells.
- Deformational flow with two slotted cylinders.

Numerical results for all these schemes are summarized in Tables 4 to 7 and on figures Figs. 1 to 4. From the numerical results we conclude the following:

- (1) All three schemes produce almost similar numerical results if flux limiters are not used in ICON-FFSL and in the adjoint scheme with artificial source term.
- (2) If flux limiters are used then ICON-FFSL scheme and adjoint scheme with artificial source term produce practically similar numerical results. Using different flux limiters has almost no effect on accuracy of computation.

- (3) The standard adjoint scheme produces larger errors compared to the ICON-FFSL scheme and the adjoint scheme with artificial source term, if flux limiters are used, see Fig. 2 and Fig. 4.
- (4) Tests are calculated on R2B4 grid with 20480 nodal points. If flux limiters are not applied then the maximum principle is violated in almost in a half of the nodal points, overshoots and undershoots result in nonphysical negative numerical values. ICON-FFSL and the adjoint with artificial source are free of these drawbacks when flux limiters are applied.

4.2.2. *Standard adjoint and adjoint with artificial source term.* In this subsection the adjoint scheme with artificial source term with flux limiters is compared with the standard adjoint scheme. Test problems featuring deformational flow and moving vortices are considered. Numerical results are given in Tables 8 to 10, and in Figs. 5 to 15. The analysis of the numerical results suggests that the adjoint scheme with artificial source term is much more accurate than the standard adjoint scheme. In particular we observe the following properties:

- (1) Standard adjoint scheme does not maintain the shape of the contours while the adjoint with artificial source is almost indistinguishable from the exact solution, see e.g. Fig. 13.
- (2) The standard adjoint scheme produces larger errors compared to adjoint scheme with artificial source term.
- (3) Maximum principle is violated by the standard adjoint scheme resulting in overshoots and undershoots and negative concentrations in almost half of nodal points of the ICON grid.
- (4) For some test problems the adjoint scheme with artificial source term with flux limiter [32], [23] also gives negative concentrations in almost a third of nodal points of the ICON grid, though negative values are of 10^{-8} magnitude at most. When flux limiter [32], [6] is used then negative concentrations appear just in 14 nodal points and it's magnitude is very small - 10^{-15} .

4.3. Data assimilation test cases.

4.3.1. *Setup for tests.* In this subsection we study established test methods in the framework of passive tracer data assimilation. We compare against each other standard adjoint, artificial source term adjoint with limiter from [32], [23] and without limiter. Numerical results of advection tests given in previous subsections have shown that standard adjoint and artificial source term adjoint without limiter produce almost similar results. Therefore for some tests one case of them only will be considered; artificial source term method with limiter is considered in all test cases. The following three combinations of initial scalar fields and velocity vectors are selected:

- (1) Moving vortices that correspond to initial scalar field 3 from Table 2 and to the vector field 4 from Table 3.
- (2) Deformational flow with cosine bells that correspond to initial scalar field 4 from Table 2 and to the vector field 3 from Table 3.
- (3) Deformational flow with slotted cylinder that correspond to initial scalar field 5 from Table 2 and to the vector field 3 from Table 3.

Notice that for selected test problems with moving vortices $div(\vec{v}) = 0$ and for the deformational flow $div(\vec{v}) \neq 0$.

Cost function (4) with discretization of the background term according to (12) and with discretization of the observation term corresponding to (13) is used in numerical tests. In this paper we do not study covariance models and the goal is development of adjoint solvers. Therefore operators K_b and K_o are set to identity operators in numerical tests. The cost function also contains the functions q_b and q_o as input. Therefore for finalizing data assimilation related test problems we define observations and background initial condition. For different test problems this is done differently, in particular, observations q_o are defined as follows:

- For numerical tests with moving vortices exact solution is known for an arbitrary time moment t and therefore the exact solution is used for defining observations in selected points in space and in time, i.e. $q_o(t_k, \xi_i) = u_{exact}(t_k, \xi_i)$, $k = 1, 2, \dots, N_T$, $i \in \mathcal{O}$.

- For numerical tests with deformational the flow exact solution is not known for an arbitrary time moment t and therefore ICON-FFSL will be used for computing a reference solution which is used for defining observations in selected points in space and in time, i.e. $q_o(t_k, x_i) = u_{ICON-FFSL}(t_k, x_i)$, $k = 1, 2, \dots, N_T$, $i \in \mathcal{O}$.

The number of observation points and their location is different for different numerical tests and therefore they are presented together with concrete numerical tests in the next subsection.

The background initial condition is constructed as an error in the true initial condition. This is done in the following way:

- For numerical tests with moving vortices the background initial condition is defined as the true initial condition plus 10 % of error in each nodal point.
- For numerical tests with deformational flow in the true initial condition the error is introduced in one half of computational domain only. For the second half of computational domain background initial condition and true initial condition coincide with each other. These domains are selected such that one cosine bell or slotted cylinder remains unchanged in the background initial condition. In those nodal points where the error is introduced and where the true initial condition is not zero background initial condition is defined as true initial condition plus 10 % of error. For the rest of nodal points of the half of computational domain 1% of maximum of the true initial condition is added.

The above procedure results in differences between true and background initial condition, details of which are given in the Table 11.

For minimizing the cost function the quasi-Newton method LBFGS [13] is used here. The developed solvers are applied for supplying gradient of the cost function in LBFGS. ICON-FFSL is used for forward runs in order to supply needed input data to adjoint solvers. Magnitude of the cost function is used as most suitable measure for comparing different adjoint solvers against each other. The difference between the true initial condition and the one found by minimization procedure can also be used where appropriate. Details on results of numerical tests are given in the next subsections.

4.3.2. Convergence of iteration process. Here we study behavior of developed adjoint solvers by means of performing 300 LBFGS iterations. We suppose 300 iterations will be enough for demonstrating convergence of iteration process. Calculations are done on ICON R2B4 grid with 5120 observation points. Observation points are distributed on the grid evenly. In case of 5120 observation points, every fourth point is observed. For the test problem with moving vortices the initial cost function is around $2.5 \cdot 10^6$ and after final iterations the cost is reduced to 131.9 for standard adjoint, to 30.7 for artificial source term adjoint with limiter and to 19.2 for artificial source term adjoint without limiter. For all three methods the progress of minimisation is illustrated on Figs. 17a to 17c. For different number of iterations situation is different: for 10 iterations best reduction of the cost function is given by standard adjoint, for 100 iterations best result is given by artificial source term adjoint and for 300 iterations best result is given by artificial source term adjoint without limiter. Oscillations visible in Fig. 17b are due to the restart in LBFGS method. Restart in minimisation is done when LBFGS algorithm reaches 5 attempts to find α step satisfying Wolfe conditions [13]. After the restart background condition is updated by the last optimized initial condition and the minimisation process starts again. The figure shows that after restart the cost the function increases first and then it decreases again. Similar behavior is observed in case of all adjoint solvers considered.

Background and observation costs are given in Fig. 17d and Fig. 17e respectively for the iterations 295-300. We see that the standard adjoint solver is better at minimizing the observation term, while the artificial source term adjoint solvers are much better in minimizing background term of the cost function. This example shows the importance of the right adjoint solvers on the minimization process: gradient defines descent direction and it is calculated using adjoint solver; therefore different adjoint solvers can lead to different priorities, e.g. which term to be reduced in the cost function.

Standard adjoint and artificial source term adjoint are numerically investigated on convergence on test problem of deformational flow with two cosine bells on ICON R2B4 grid with 5120 observation points. Initial cost function is around $3.5 \cdot 10^4$ and after 300 iterations the cost is reduced to 2.2 for standard adjoint

solver and to $4 \cdot 10^{-2}$ for artificial source term adjoint solver. Both methods ensure convergence, the process is illustrated on Figs. 16a to 16c. Before 30 iterations standard adjoint gives better results and after 30 iterations cost function corresponding to artificial source term adjoint is smaller. In this test problem we do not observe a similar effect as in previous test problem behavior in the quest for prioritisation of the observation or background term. Both methods minimize background and observation terms of the cost function in the similar way.

These numerical results suggest that for the selected test problems all considered adjoint solvers ensure convergence of iteration process, initial cost function is reduced approximately 10^5 times after 300 iterations and those adjoint solvers that give best reduction of the cost function after 300 iterations are different from those which give better results for smaller number, e.g. 10 iterations.

4.3.3. Impact of number of observations. We study numerically three test problems given in the subsection 4.3.1. Calculations are done on ICON R2B4 grid with 2560, 5120, 10240 and 20480 observation points for 50 LBFGS iterations. Notice that R2B4 grid contains 20480 nodal points, i.e. we also consider the idealized case when observations are given in all nodal points of the grid. Numerical results are given in Fig. 18a for tests with moving vortexes, in the Fig. 18b for tests with deformational flow and cosine bells, in the Fig. 18c for tests with deformational flow and slotted cylinders. These results suggest the following:

- In case of using standard adjoint solver the cost function monotonically increases together with the number of observation points for tests with deformational flow. For tests with moving vortices cost function first decreases for 5120 observation points and then it increases monotonically together with number of observation points.
- In case of using artificial source term adjoint solver with limiter the cost function decreases together with the number of observation points for tests with deformational flow and cosine bells. For a deformational flow with slotted cylinders the cost function increases for 20480 observation points though the growth is not as dramatic as in case of using standard adjoint solver. For tests with moving vortices cost function also decreases though we observe oscillations and peaks for 10240 observation points.

Numerical results suggest that the efficiency of iterations decreases when increasing number of observation points, i.e. for the same number of iterations we get a larger cost function in case of more observation points. Using different adjoint solvers influences minimization process differently and the adjoint solver with artificial source term offers more reliable behavior when increasing number of observation points.

4.3.4. Effect of mesh refinement. Mesh refinement is a standard procedure for studying numerically convergence of numerical methods. As a result of mesh refinement accuracy increases for convergent methods. Namely ICON FFSL and its descendant adjoint solvers should produce more accurate solutions on refined meshes. Here we study the effect of mesh refinement on selected test problems in the context of variational data assimilation. In numerical tests given in previous subsections the R2B4 grid was used. Here we consider sequence of grids R2B4, R2B5, R2B6, R2B7 with 20480 observation points. Corresponding cost functions are given in Table 12. We observe that the final cost function increases together with the mesh refinement since we keep same number of observation points for all meshes. Notice that for each test problem the starting value of cost function is almost the same for all meshes. Though after 50 iterations we observe large difference in cost function evolution as impact of using different adjoint solvers. Namely for the same number of iterations the artificial source term adjoint solver with limiter yields cost function values which are from 8 to 660 times smaller than cost functions obtained with the adjoint solver without limiter.

4.3.5. Manipulating weights of background and observation terms. Weights can be used for prioritizing the background or observation term in the cost function. In numerical tests considered in previous subsections the weight was set to 0.5 for both terms. Here in numerical tests we gradually increase the relative weight of observation term up to 1 and at the same time we decrease weight of background term down to 0. Corresponding cost functions on R2B4 grid for 50 LBFGS iterations and 5120 observation points are given on Figs. 19a to 19c. These figures suggest the following:

- For tests with moving vortices cost functions decrease when weight of observation term increases. Cost function values calculated by artificial source term solver without limiter is smaller then cost function with the same solver using a limiter, namely when background term disappears, i.e. weight of observation term is 1, we have $J_{o,Art.S.NoLimiter}/J_{o,Art.S.WithLimiter} = 0.248777957$.
- For tests with deformational flow and cosine bells cost function values decrease when the weight of observation term increases. Cost function values calculated by artificial source term solver with limiter is smaller then cost function produced by standard adjoint solver, we have $J_{o,Std.Adjoint}/J_{o,Art.S.WithLimiter} = 1.878180425$.
- For tests with deformational flow and slotted cylinders cost functions increase together with weight of observation term. If the standard adjoint solver is used the growth of the cost function is faster and its value is also bigger compared to the case when the artificial source term adjoint with limiter is used, $J_{o,Std.Adjoint}/J_{o,Art.S.WithLimiter} = 58.210774364$.

In case when the background term disappears in the cost function the true initial scalar field can be compared with those found by data assimilation. The results are given in the Table 11. They suggest the following

- For tests with moving vortices some error norms are approximately two times smaller in case of using artificial source term adjoint without limiter compared to the same solver with limiter.
- For tests with deformational flow and cosine bells the standard adjoint solver gives better result compared to artificial source term adjoint solver with limiter, namely in $l_1, l_{1,rel}, l_2, l_{2,rel}$ norms error is slightly smaller and for $l_\infty, l_{\infty,rel}$ norms the error is approximately 3 times smaller.
- For tests with deformational flow and slotted cylinders using the adjoint solver with artificial source term with limiter gives approximately 7 times smaller error norms compared to the case when standard adjoint solver is used.

Putting together Figs. 19a to 19c and Table 11 we conclude that value of cost function is a good indicator for comparing adjoint solvers in the sense that if the cost function is smaller, then the solution of the variational data assimilation better approximates the true initial condition. We observe this behavior in case of numerical tests considered with moving vortices and slotted cylinders. For the test problem with cosine bells this conclusion is not valid for 5120 observations and it is true for 20480 observations.

5. CONCLUSIONS

We considered two approaches for developing adjoints of ICON-FFSL schemes for the linear advection equation in the ICON model. The first approach is standard and it is used for building the adjoint of ICON-FFSL scheme without flux limiters. Another approach is new and it is used for constructing the adjoint scheme of ICON-FFSL with or without flux limiters. The new approach is based on rewriting the adjoint equation in flux form using an artificial source term and then using the same discretization method as its parent ICON-FFSL scheme. Because of this feature the development of adjoint solver is easy and very fast if, as it is typically the case, the parent forward solver is available. Another advantage is that flux limiters can be applied in our artificial source term method in a straightforward way thus ensuring stability regardless of smoothness of the solution. Stability and consistency of the adjoint scheme is proved under assumption that the parent scheme has these properties. ICON-FFSL and its descendant adjoint solvers are compared against each other on a collection of standard advection test cases and variational data assimilation test cases developed here. For some test cases when the solution is smooth, the adjoint solvers without limiter can provide competitive and even smaller errors. For other and more realistic of test cases the artificial source term solver with limiter is the clear winner ensuring reduction of the cost function even in cases where adjoint solvers without limiter fail to perform minimization.

6. APPENDICES

6.1. Input for tests: initial condition and wind field.

Table 2 Initial scalar fields

No	Initial scalar field	Parameters	Source
1	Cosine bell $q(\lambda, \theta, t_0) = \begin{cases} \frac{h_{max}}{2} (1 + \cos \frac{\pi r}{\tilde{r}}), & \text{if } r < \tilde{r} \\ 0, & \text{otherwise} \end{cases}$	$r = \arccos(\sin \theta_c \sin \theta + \cos \theta_c \cos \theta \cos(\lambda - \lambda_c))$ $h_{max} = 1 \quad \tilde{r} = 1/3 \quad (\lambda_c, \theta_c) = (3\pi/2, 0)$	[31]
2	Slotted cylinder $q(t_0, \lambda, \theta) = \begin{cases} c, & \text{if } r \leq \tilde{r}, \lambda - \lambda_c \geq \frac{\tilde{r}}{6}, \\ c, & \text{if } r \leq \tilde{r}, \lambda - \lambda_c < \frac{\tilde{r}}{6}, \quad \theta - \theta_c < \frac{2}{3}\tilde{r}, \\ b, & \text{otherwise} \end{cases}$	$r = \arccos(\sin \theta_c \sin \theta + \cos \theta_c \cos \theta \cos(\lambda - \lambda_c))$ $\tilde{r} = 1/2$ $c = 1 \quad b = 0 \quad (\lambda_c, \theta_c) = (3\pi/2, 0)$	[32]
3	Vortex $q(t_0, \lambda', \theta') = 1 - \tanh\left[\frac{\tilde{r}}{\gamma} \sin(\lambda' - \omega(\theta')t)\right]$	$\lambda'(\lambda, \theta) = \arctan\left[\frac{\cos \theta \sin(\lambda - \lambda_p)}{\cos \theta \sin \theta_p \cos(\lambda - \lambda_p) - \cos \theta_p \sin \theta}\right],$ $\theta'(\lambda, \theta) = \arcsin[\sin \theta \sin \theta_p + \cos \theta \cos \theta_p \cos(\lambda - \lambda_p)],$ $\omega(\theta') = \begin{cases} V/(R\tilde{\rho}), & \text{if } \tilde{\rho} \neq 0, \\ 0, & \text{otherwise.} \end{cases}$ $V = v_0 \frac{3\sqrt{3}}{2} \operatorname{sech}^2(\tilde{\rho}) \tanh(\tilde{\rho})$ $v_0 = 2\pi R/T \quad \tilde{\rho} = \tilde{\rho}_0 \cos \theta'$ $R = 6.371229 \times 10^6 [m] \quad T = 1036800 [s]$ $(\lambda_p, \theta_p) = (\pi - 0.8 + \pi/4, \pi/4.8)$ $\gamma = 5 \quad \tilde{\rho}_0 = 3$	[18]
4	Two cosine bells $q(t_0, \lambda, \theta) = \begin{cases} b + ch_1(\lambda, \theta), & \text{if } r_1 < \tilde{r}, \\ b + ch_2(\lambda, \theta), & \text{if } r_2 < \tilde{r}, \\ b, & \text{otherwise,} \end{cases}$	$h_i(\lambda, \theta) = \begin{cases} \frac{h_{max}}{2} (1 + \cos \frac{\pi r}{\tilde{r}}), & \text{if } r_i < \tilde{r} \\ 0, & \text{otherwise} \end{cases}$ $r_i = \arccos(\sin \theta_{c,i} \sin \theta + \cos \theta_{c,i} \cos \theta \cos(\lambda - \lambda_{c,i}))$ $i = 1, 2 \quad h_{max} = 1 \quad \tilde{r} = 1/2 \quad c = 1 \quad b = 0$ $(\lambda_{c,1}, \theta_{c,1}) = (3\pi/4, 0) \quad (\lambda_{c,2}, \theta_{c,2}) = (5\pi/4, 0)$	[31]
5	Two slotted cylinders $q(t_0, \lambda, \theta) = \begin{cases} c, & \text{if } r_i \leq \tilde{r}, \lambda - \lambda_{c,i} \geq \frac{\tilde{r}}{6} \text{ for } i = 1, 2, \\ c, & \text{if } r_1 \leq \tilde{r}, \lambda - \lambda_{c,1} < \frac{\tilde{r}}{6}, \quad \theta - \theta_{c,1} < -\frac{5}{12}\tilde{r}, \\ c, & \text{if } r_2 \leq \tilde{r}, \lambda - \lambda_{c,2} < \frac{\tilde{r}}{6}, \quad \theta - \theta_{c,2} > \frac{5}{12}\tilde{r}, \\ b, & \text{otherwise,} \end{cases}$	$r_i = \arccos(\sin \theta_{c,i} \sin \theta + \cos \theta_{c,i} \cos \theta \cos(\lambda - \lambda_{c,i}))$ $i = 1, 2 \quad \tilde{r} = 1/2 \quad c = 1 \quad b = 0$ $(\lambda_{c,1}, \theta_{c,1}) = (3\pi/4, 0) \quad (\lambda_{c,2}, \theta_{c,2}) = (5\pi/4, 0)$	[17]

Table 3 Velocity vector

No	Velocity vector	Parameters	Source
1	Solid body rotation: $\nabla \cdot \vec{v} = 0$ Exact solution: after complete revolution, initial field reaches starting position		
	$v_\lambda(\lambda, \theta) = u_0(\cos \theta \cos \alpha + \sin \theta \cos \lambda \sin \alpha),$ $v_\theta(\lambda, \theta) = -u_0 \sin \lambda \sin \alpha$	$u_0 = 2\pi R/T$ $R = 6.371229 \times 10^6[m]$ $T = 1036800[s]$ $\alpha = 0^\circ$ $0 \leq t \leq T$	[31]
2	Deformational flow: $\nabla \cdot \vec{v} = 0$ Exact solution: after complete revolution, initial field reaches starting position		
	$v_\lambda(\lambda, \theta, t) = k \sin^2(\lambda/2) \sin(2\theta) \cos(\pi t/T),$ $v_\theta(\lambda, \theta, t) = \frac{k}{2} \sin \lambda \cos \theta \cos(\pi t/T)$	$k = 2.4$ $0 \leq t \leq T$	[17]
3	Deformational flow: $\nabla \cdot \vec{v} \neq 0$ Exact solution: after complete revolution, initial field reaches starting position		
	$v_\lambda(\lambda, \theta, t) = -k \sin^2(\lambda/2) \sin(2\theta) \cos^2 \theta \cos(\pi t/T),$ $v_\theta(\lambda, \theta, t) = \frac{k}{2} \sin \lambda \cos^3 \theta \cos(\pi t/T)$	$k = 1$ $0 \leq t \leq T$	[17]
4	Moving vortices: $\nabla \cdot \vec{v} = 0$ Exact solution: Forward- $q(t, \lambda, \theta) = 1 - \tanh[\frac{\tilde{\rho}}{\gamma} \sin(\lambda' - \omega t)]$, Backward- $q(t, \lambda, \theta) = 1 - \tanh[\frac{\tilde{\rho}}{\gamma} \sin(\lambda' + \omega t)]$		
	$v_\lambda(t, \lambda, \theta) = u_0(\cos \theta \cos \alpha + \sin \theta \cos \lambda \sin \alpha) +$ $R\omega(\theta')(\sin \theta_c \cos \theta - \cos \theta_c \cos(\lambda - \lambda_c) \sin \theta),$ $v_\theta(t, \lambda, \theta) = -u_0 \sin \lambda \sin \alpha, + R\omega(\theta')(\cos \theta_c \sin(\lambda - \lambda_c)).$	$V = v_0 \frac{3\sqrt{3}}{2} \text{sech}^2(\tilde{\rho}) \tanh(\tilde{\rho})$ $v_0 = 2\pi R/T$ $\tilde{\rho} = \tilde{\rho}_0 \cos \theta'$ $\tilde{\rho}_0 = 3$ $R = 6.371229 \times 10^6[m]$ $T = 1036800[s]$ $\omega(\theta') = \begin{cases} V/(R\tilde{\rho}), & \text{if } \tilde{\rho} \neq 0, \\ 0, & \text{otherwise.} \end{cases}$ $(\lambda_c, \theta_c) = (\lambda_p + \omega t_n, \theta_p)$ $(\lambda_p, \theta_p) = (\pi - 0.8 + \pi/4, \pi/4.8)$ $t_n = n\Delta t$ $\Delta t = 600[s]$ $0 \leq t \leq T$	[16]

6.2. Numerical results of advection tests.

6.2.1. Figures for advection tests.

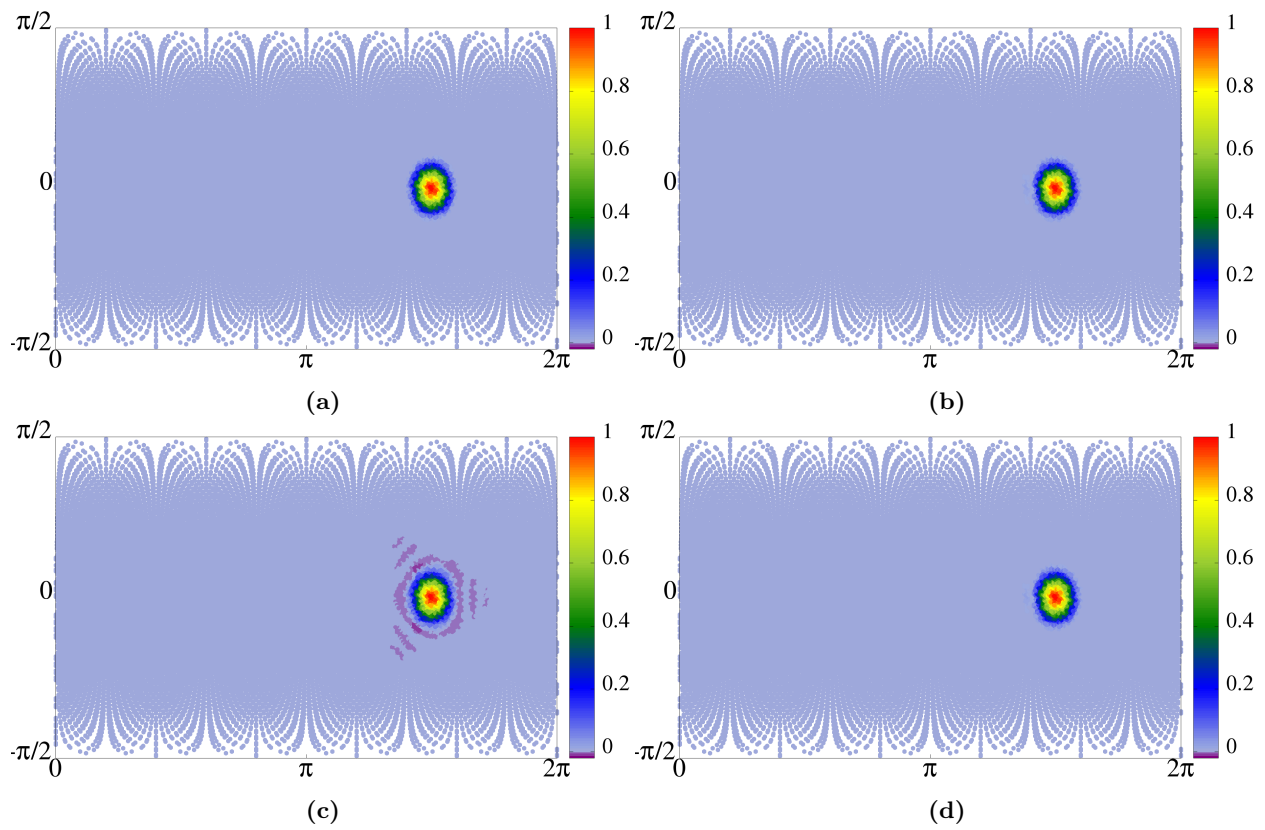


Fig. 1 Solid body rotation, cosine bell, a)-d) - contour plots with color bar: a) exact solution b) ICON-FFSL, limiter [32], [6] c) standard adjoint d) art. source adjoint, limiter [32], [6]

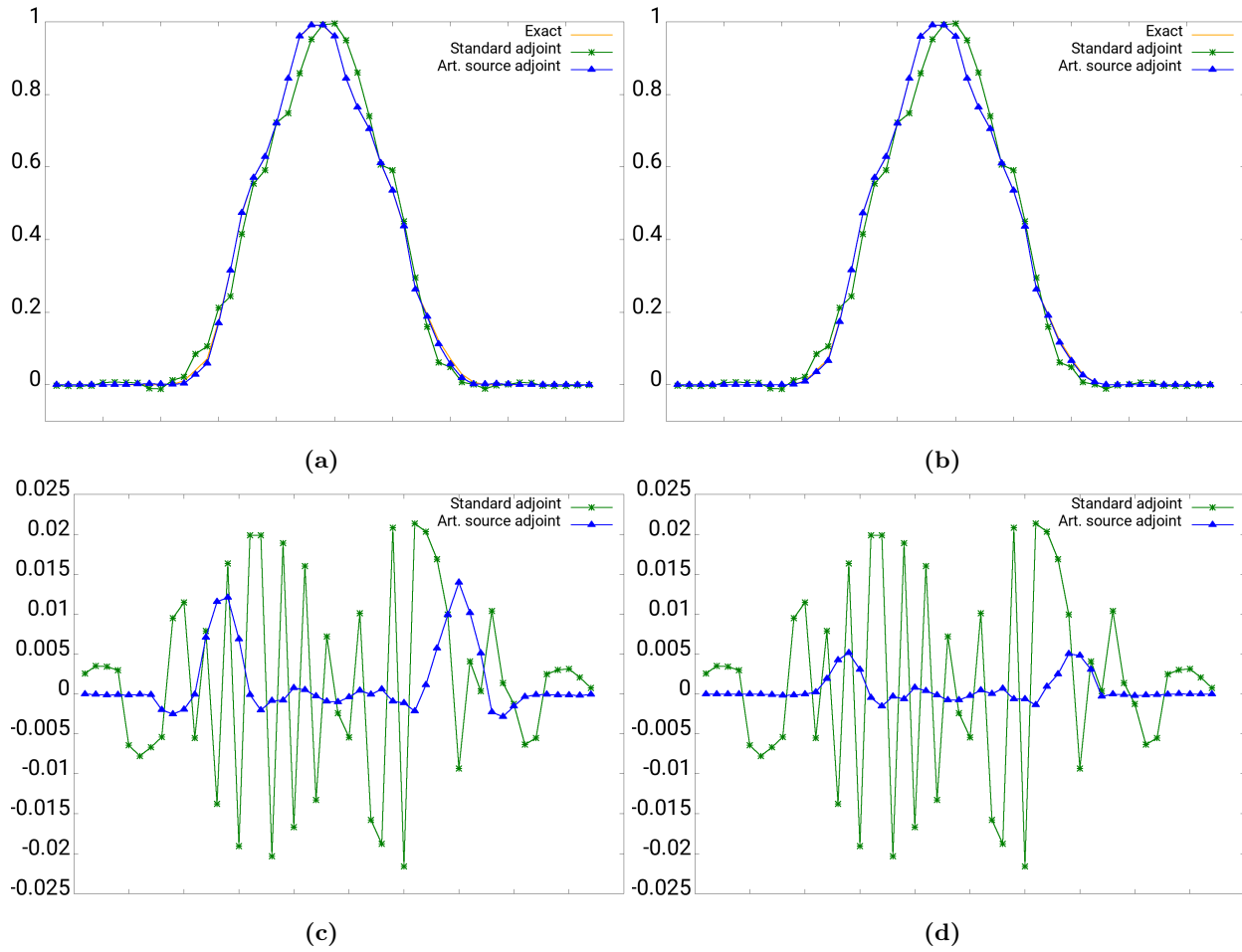


Fig. 2 Solid body rotation, cosine bell, a)-d) - along the curve exact vs standard adjoint vs art. source adjoint : a) solutions, art. source with limiter [32], [23] b) solutions, art. source with limiter [32], [6] c) errors, art. source with limiter [32], [23] d) errors, art. source with limiter [32], [6]

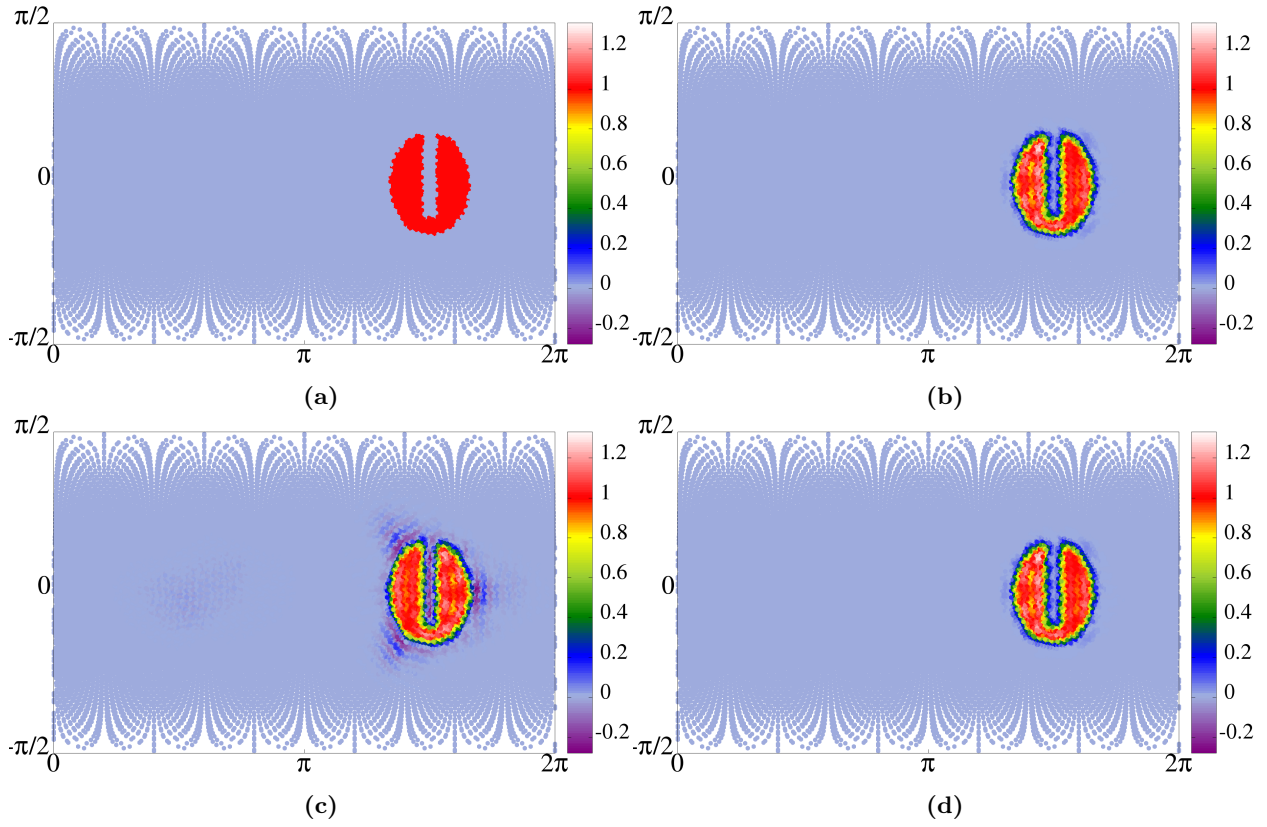


Fig. 3 Solid body rotation, slotted cylinder, a)-d) - contour plots with color bar: a) exact solution b) ICON-FFSL, limiter [32], [23] c) standard adjoint d) art. source adjoint, limiter [32], [23]

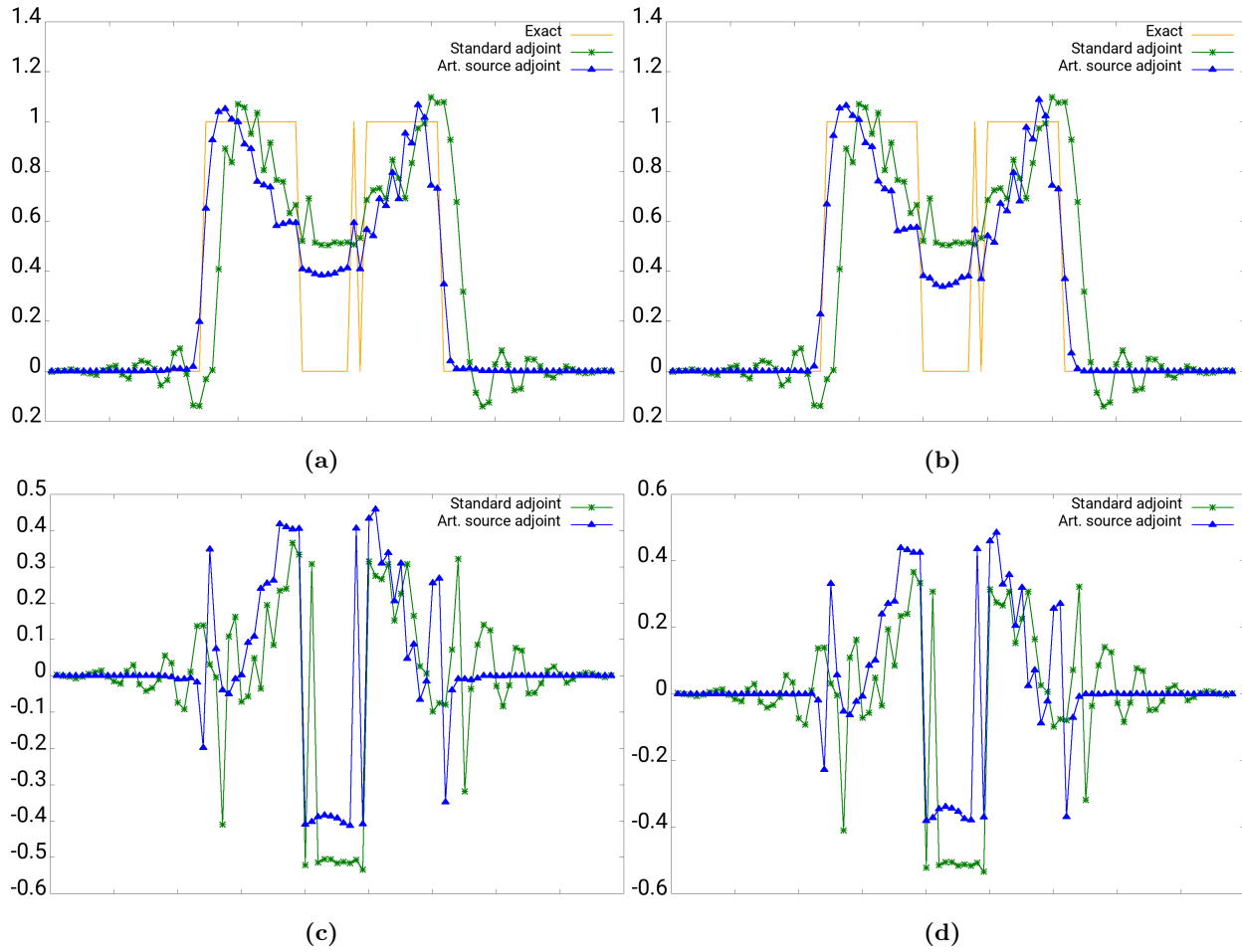


Fig. 4 Solid body rotation, slotted cylinder, a)-d) - along the curve exact vs standard adjoint vs art. source adjoint: a) solutions, art. source with limiter [32], [23] b) solutions, art. source with limiter [32], [6] c) errors, art. source with limiter [32], [23] d) errors, art. source with limiter [32], [6]

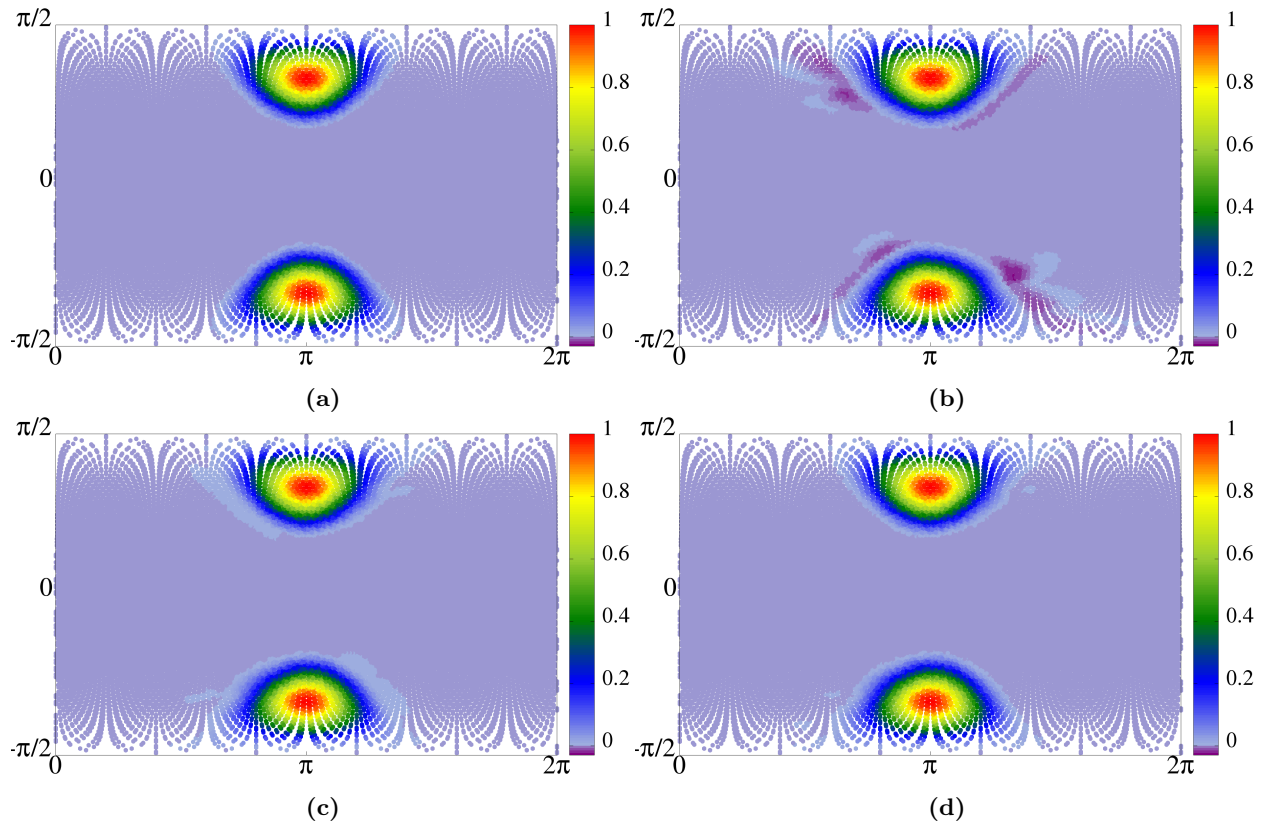


Fig. 5 Deformational flow, $\nabla \vec{v} = 0$, cosine bells, a)-d) - contour plots with color bar: a) exact solution b) standard adjoint, c) art. source adjoint, limiter [32], [23] d) art. source adjoint, limiter [32], [6]

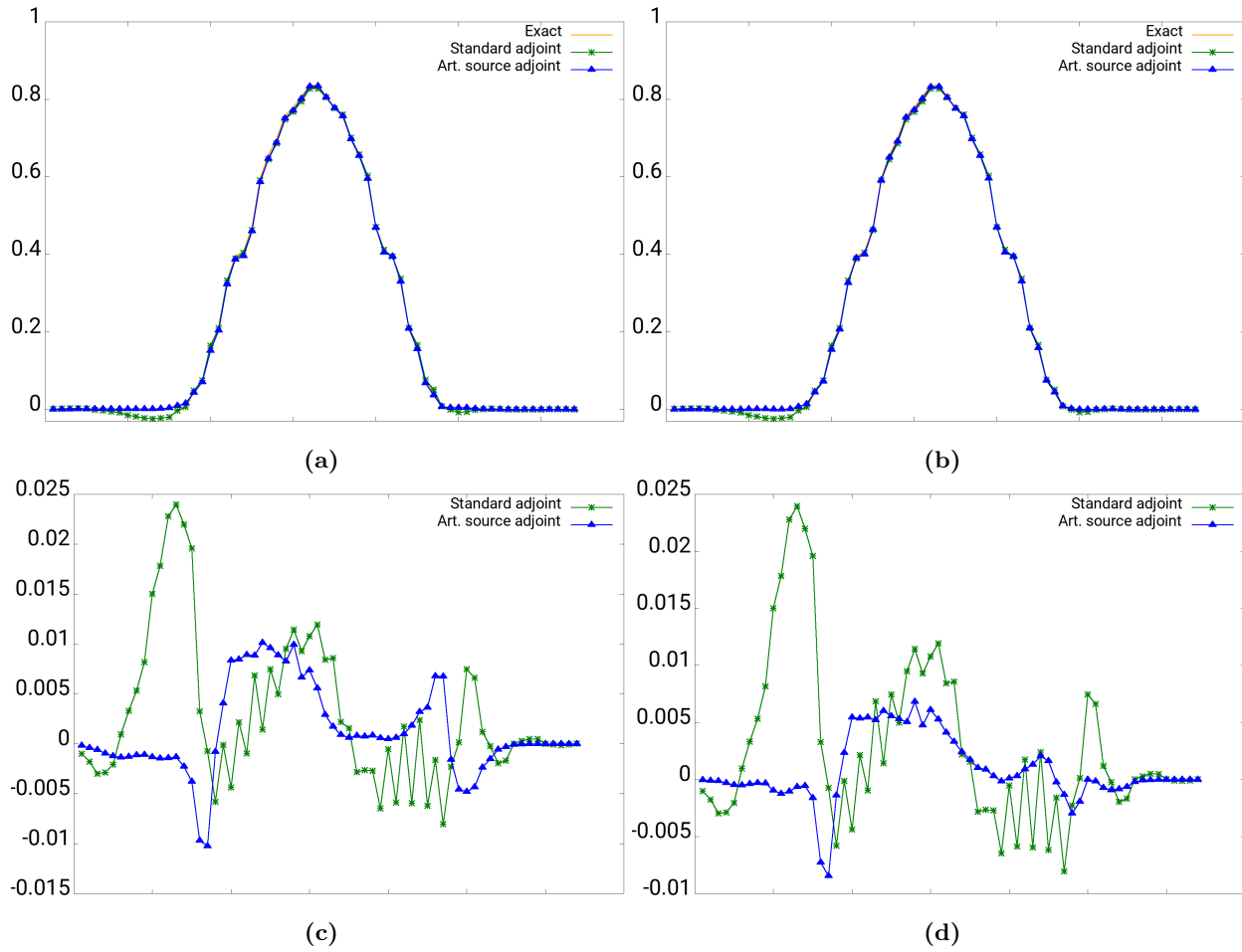


Fig. 6 Deformational flow, $\nabla \vec{v} = 0$, cosine bells, a)-d) - along the curve exact vs standard adjoint vs art. source adjoint: a) solutions, art. source with limiter [32], [23] b) solutions, art. source with limiter [32], [6] c) errors, art. source with limiter [32], [23] d) errors, art. source with limiter [32], [6]

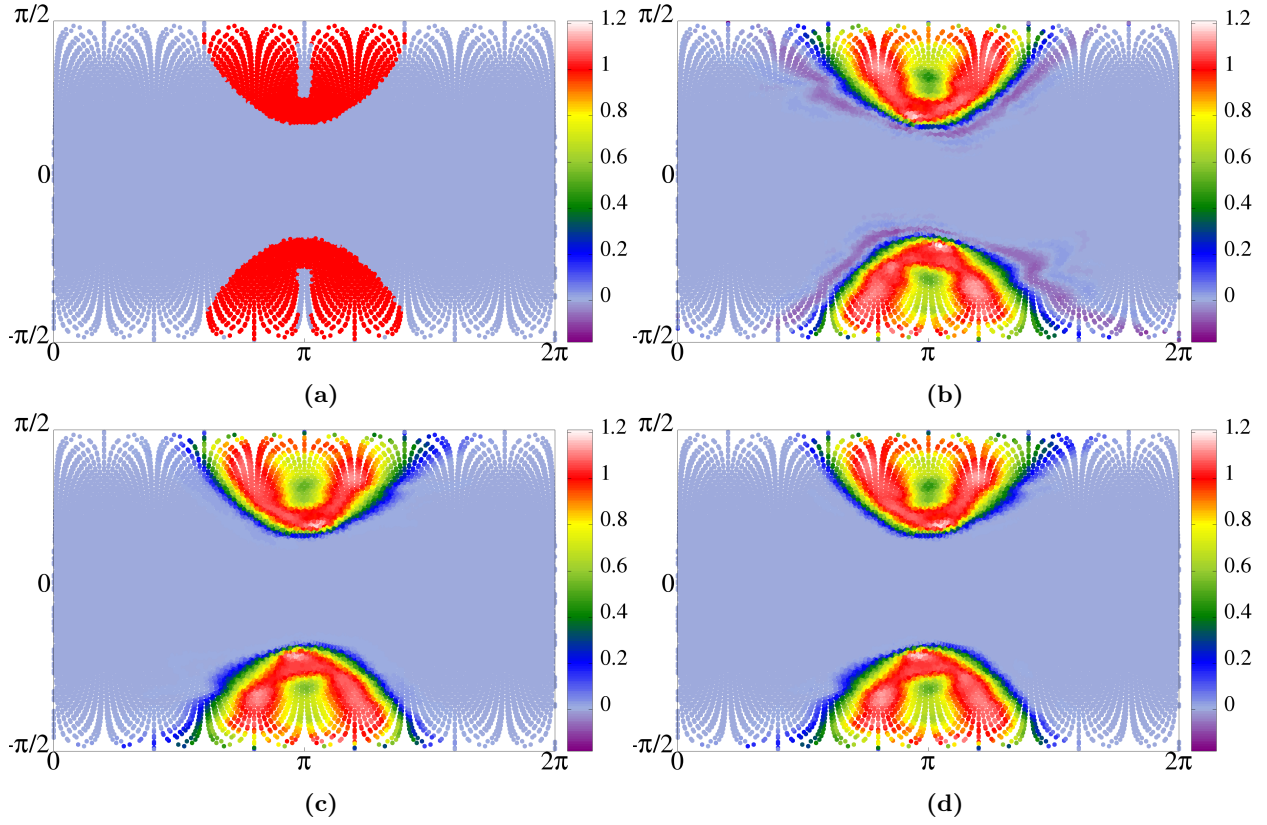


Fig. 7 Deformational flow, $\nabla \vec{v} = 0$, slotted cylinders, a)-d) - contour plots with color bar: a) exact solution b) standard adjoint, c) art. source adjoint, limiter [32], [23] d) art. source adjoint, limiter [32], [6]

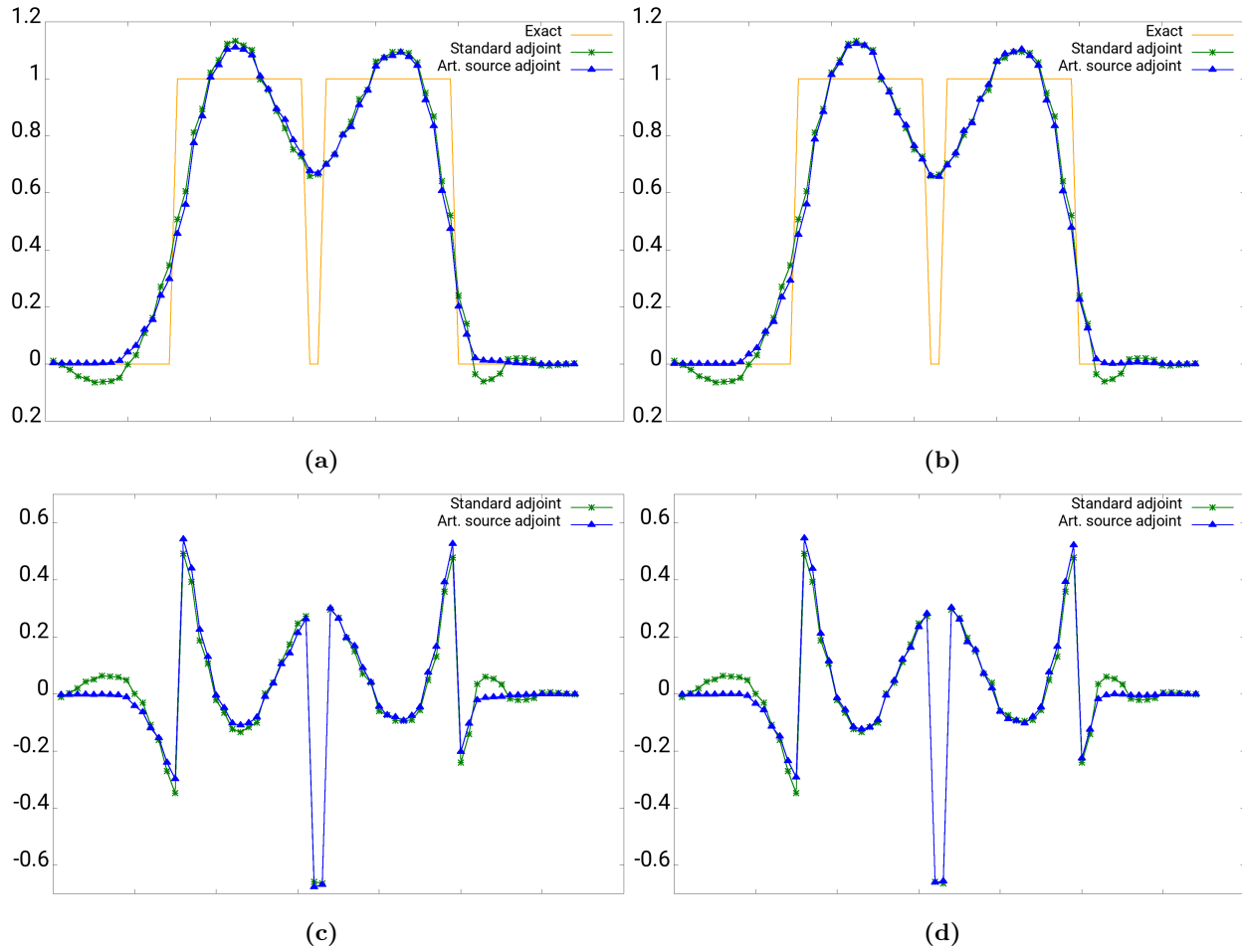


Fig. 8 Deformational flow, $\nabla \vec{v} = 0$, slotted cylinders, a)-d) - along the curve exact vs standard adjoint vs art. source adjoint: a) solutions, art. source with limiter [32], [23] b) solutions, art. source with limiter [32], [6] c) errors, art. source with limiter [32], [23] d) errors, art. source with limiter [32], [6]

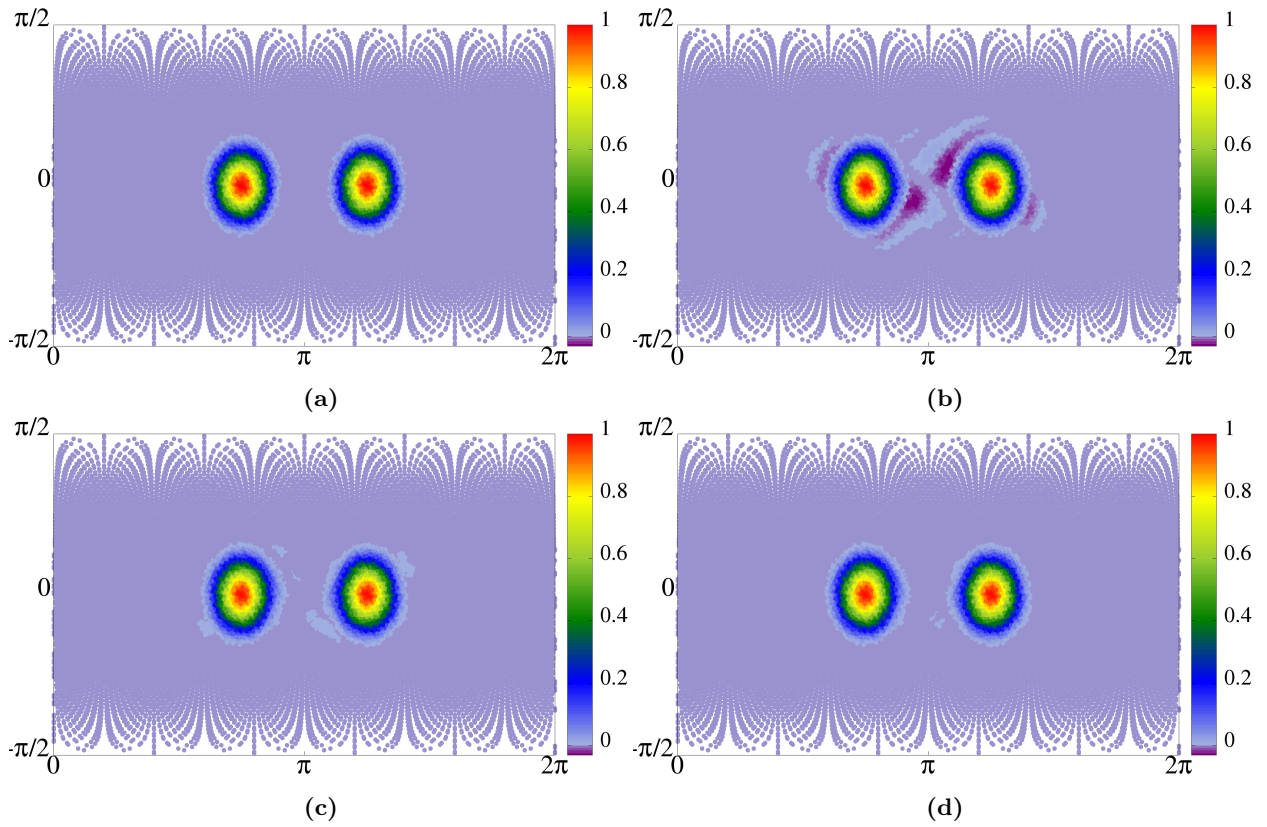


Fig. 9 Deformational flow, $\nabla \vec{v} \neq 0$, cosine bells, a)-d) - contour plots with color bar: a) exact solution b) standard adjoint, c) art. source adjoint, limiter [32], [23] d) art. source adjoint, limiter [32], [6]

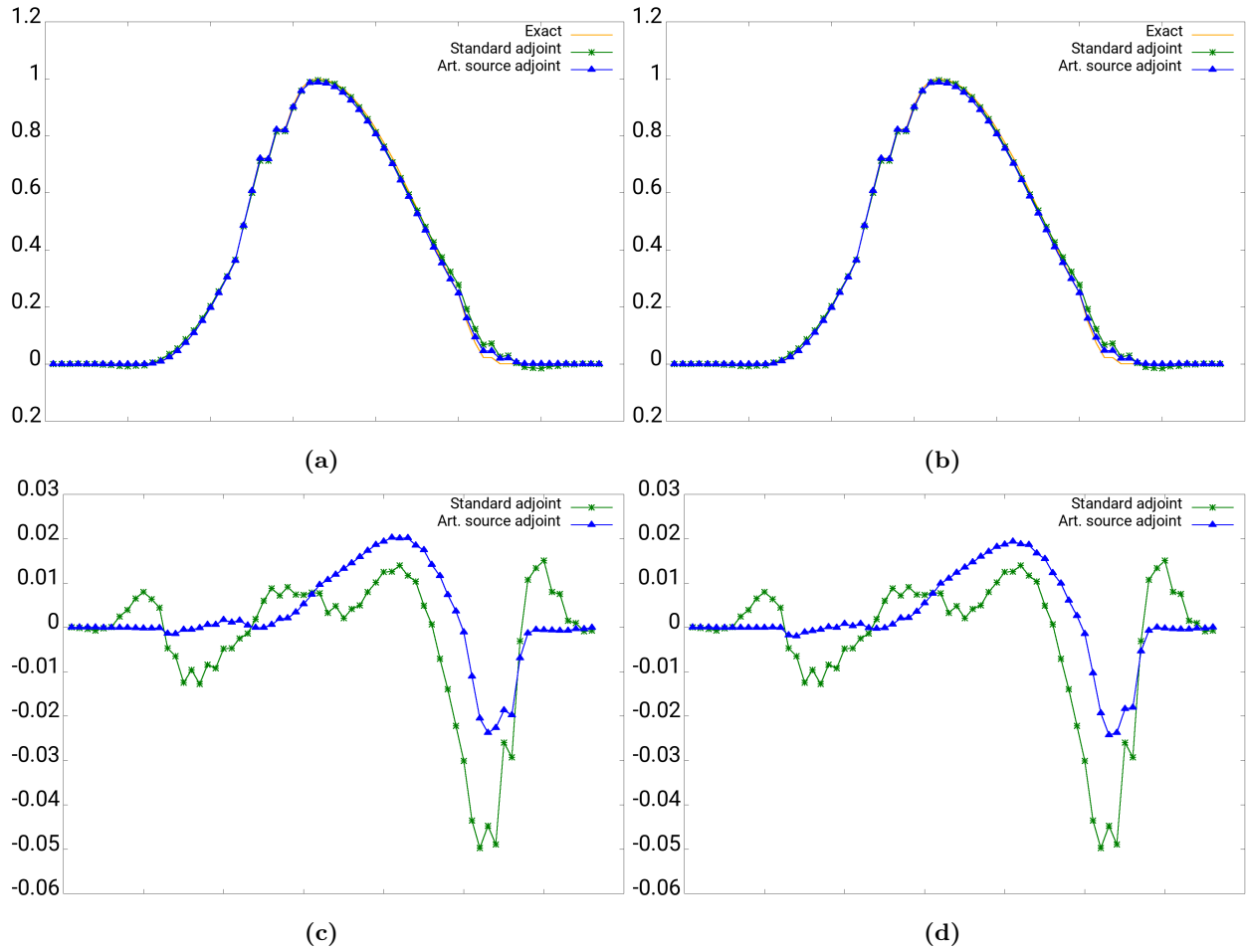


Fig. 10 Deformational flow, $\nabla \vec{v} \neq 0$, cosine bells, a)-d) - along the curve exact vs standard adjoint vs art. source adjoint: a) solutions, art. source with limiter [32], [23] b) solutions, art. source with limiter [32], [6] c) errors, art. source with limiter [32], [23] d) errors, art. source with limiter [32], [6]

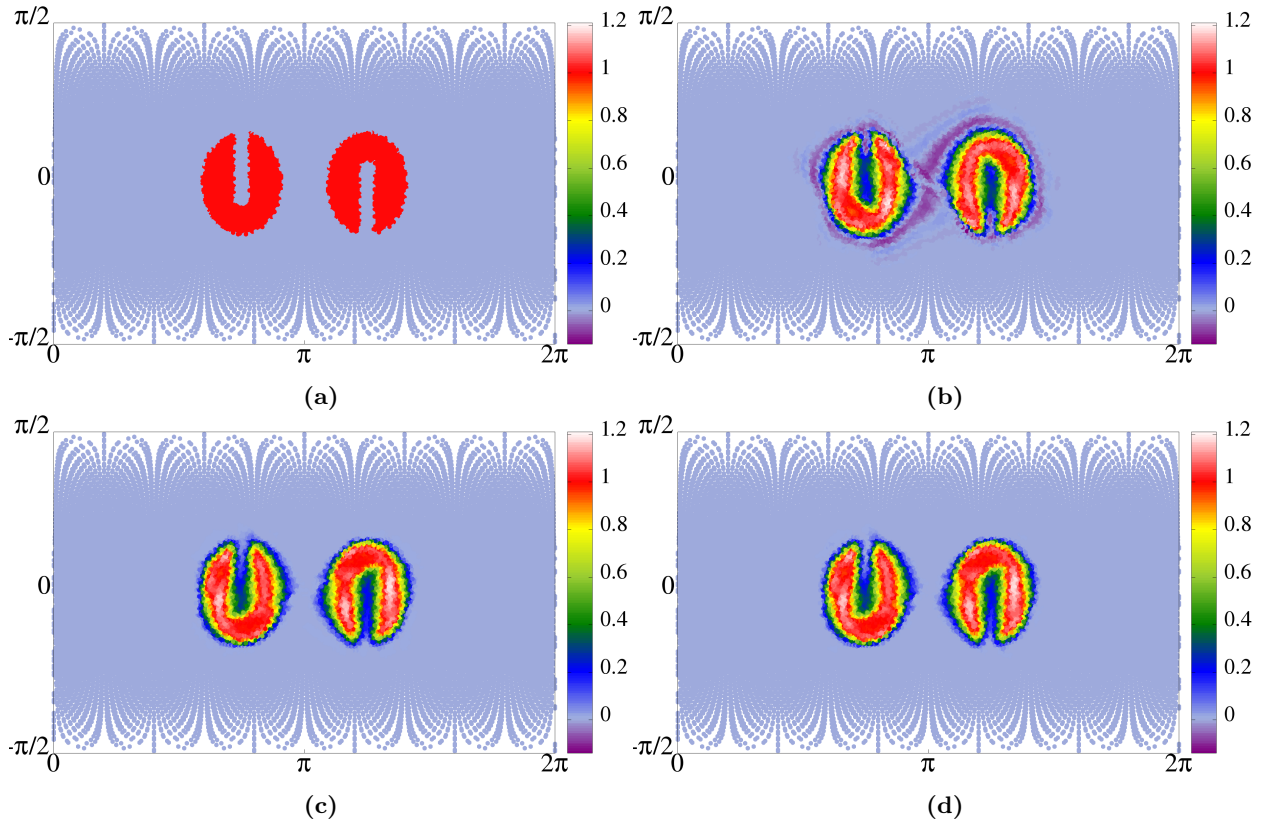


Fig. 11 Deformational flow, $\nabla \vec{v} \neq 0$, slotted cylinders, a)-d) - contour plots with color bar: a) exact solution b) standard adjoint, c) art. source adjoint, limiter [32], [23] d) art. source adjoint, limiter [32], [6]

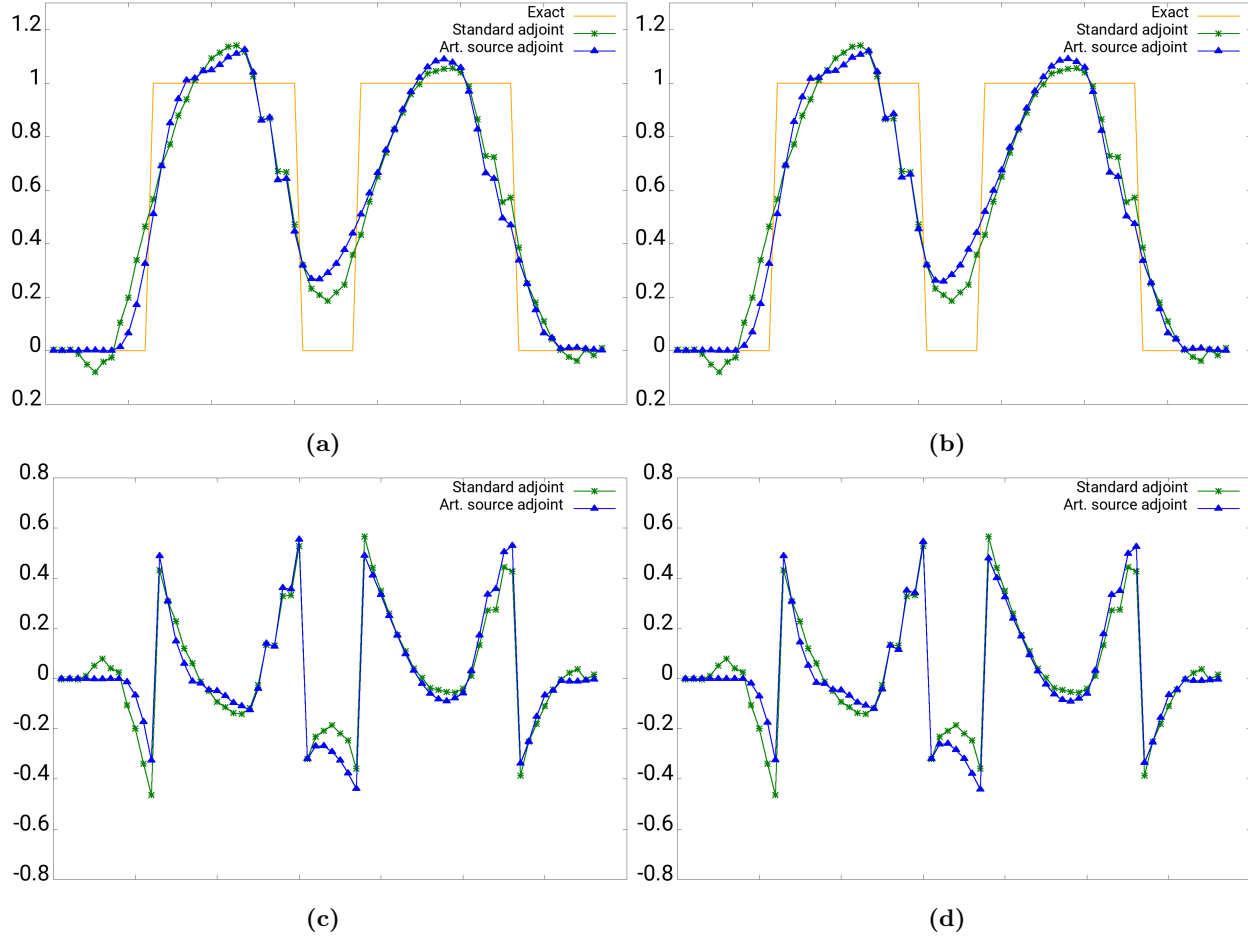


Fig. 12 Deformational flow, $\nabla \bar{v} \neq 0$, slotted cylinders, a)-d) - along the curve exact vs standard adjoint vs art. source adjoint : a) solutions, art. source with limiter [32], [23] b) solutions, art. source with limiter [32], [6] c) errors, art. source with limiter [32], [23] d) errors, art. source with limiter [32], [6]

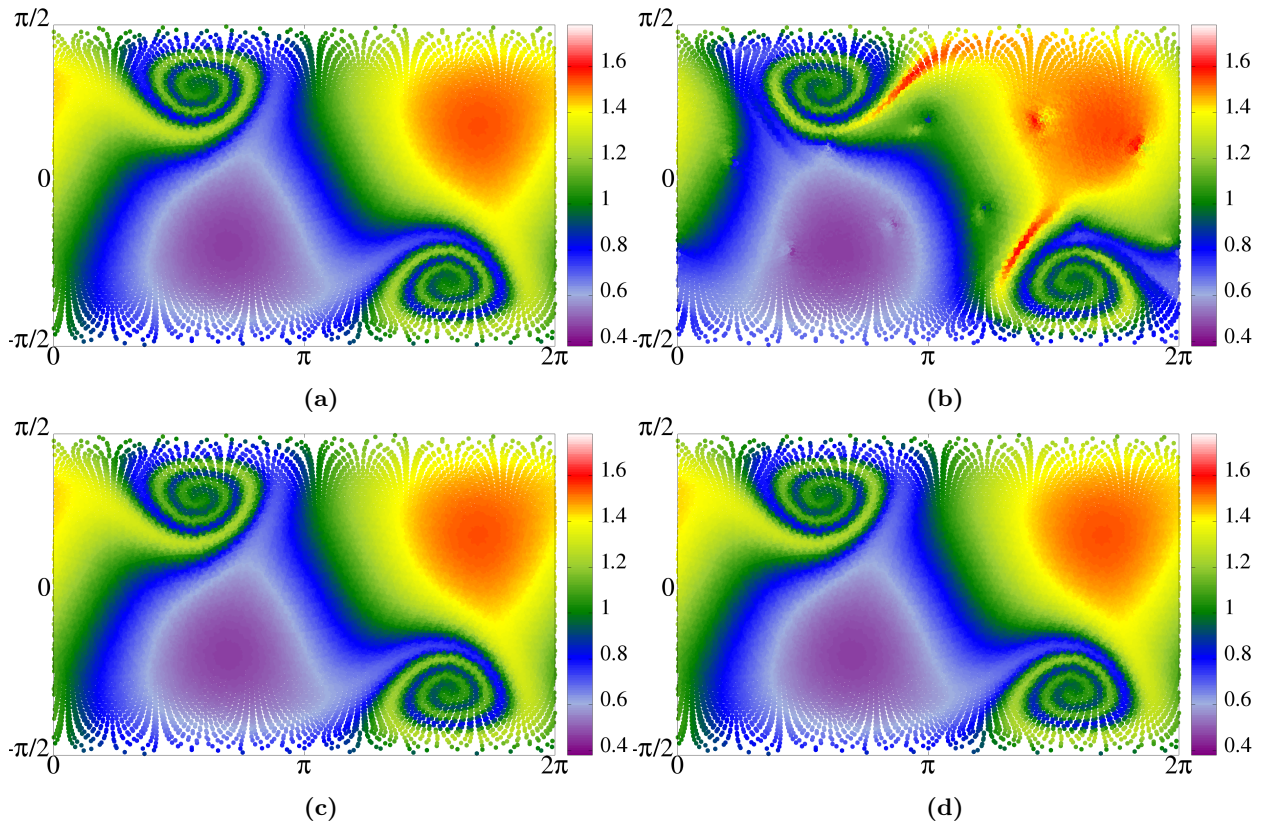


Fig. 13 Moving vortices, a)-d) - contour plots with color bar: a) exact solution b) standard adjoint, c) art. source adjoint, limiter [32], [23] d) art. source adjoint, limiter [32], [6]

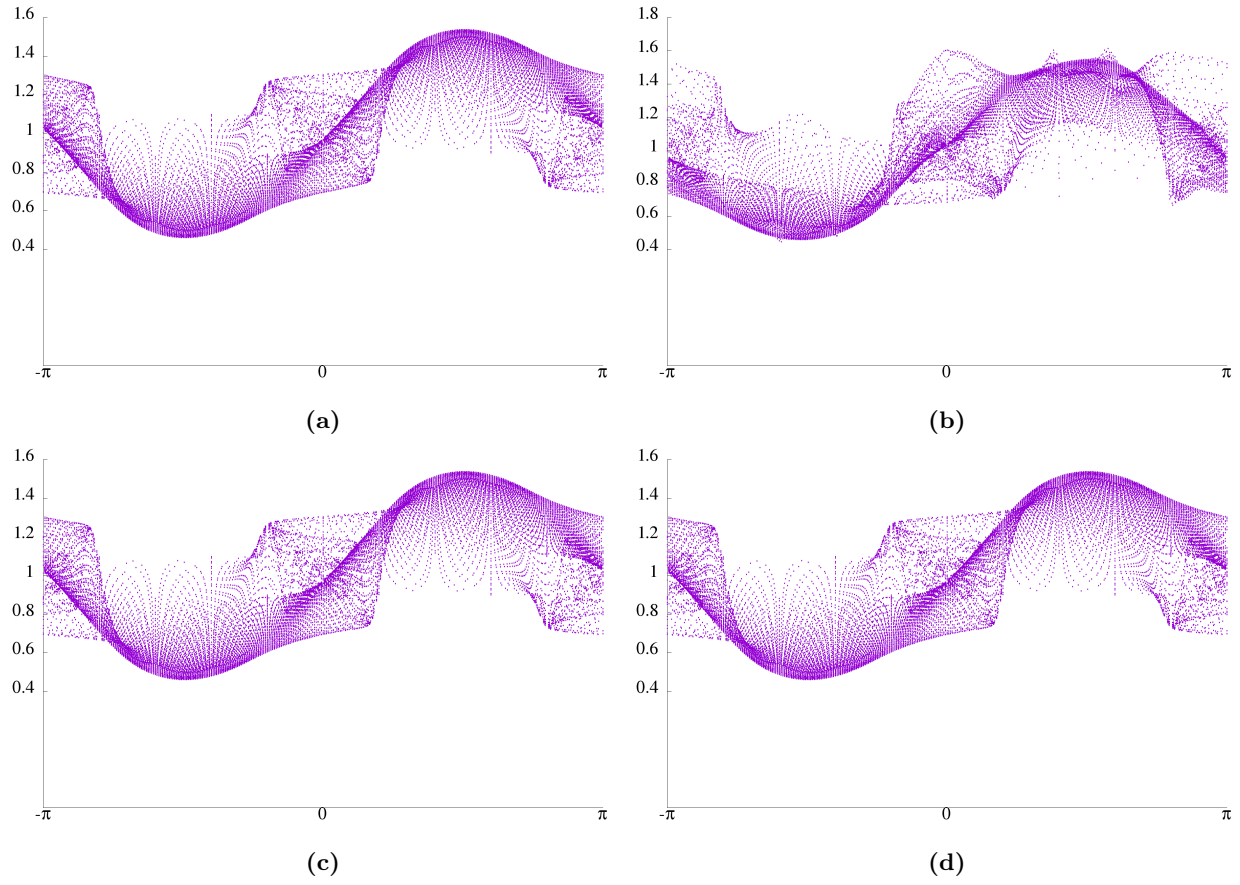


Fig. 14 Moving vortices, a)-d) - unrotated grid $(\lambda, \theta) \in [-\pi; \pi] \times [-\pi/2; \pi/2]$, plot viewing angle $(90^\circ, 0^\circ)$: a) exact solution b) standart adjoint c) art. source adjoint, limiter [32], [23] d) art. source adjoint, limiter [32], [6]

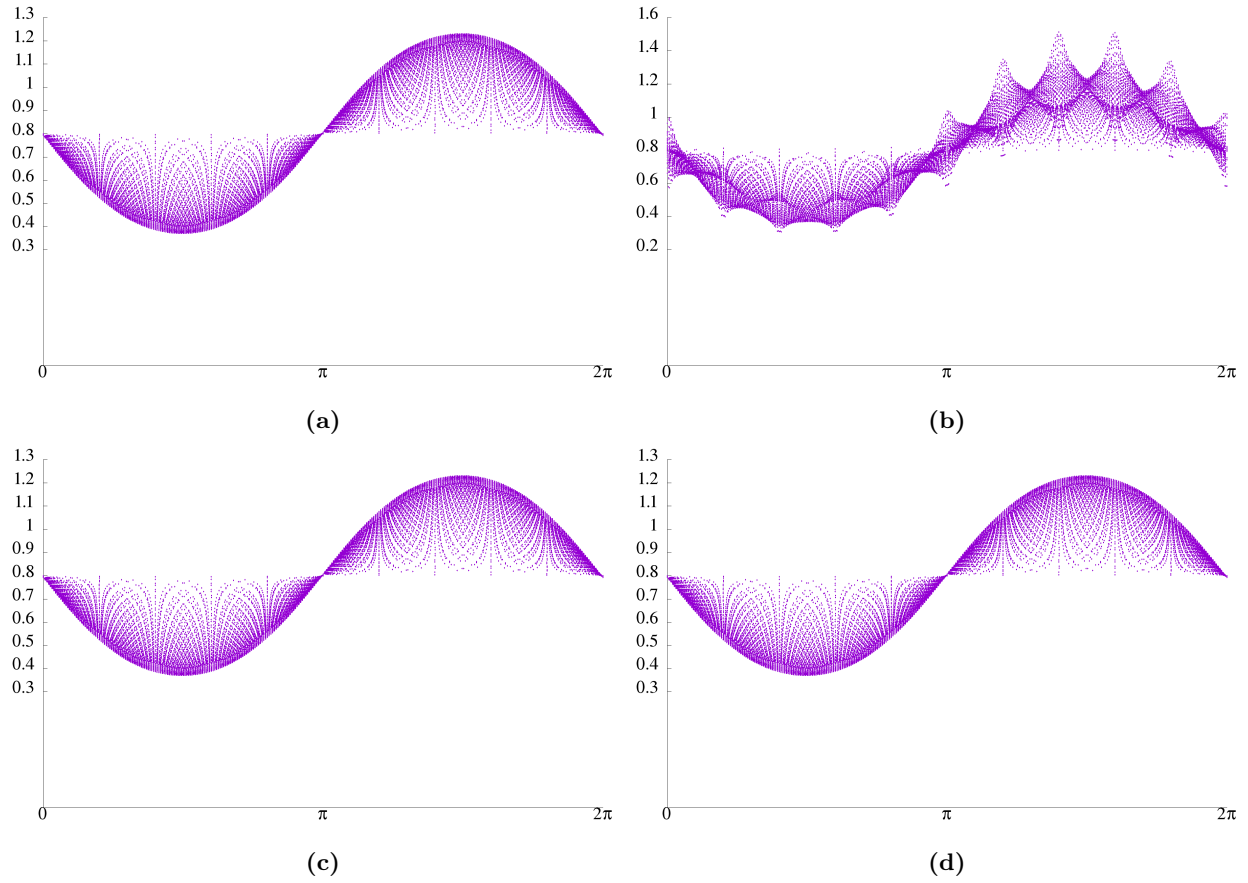


Fig. 15 Solid body rotation wind field, moving vortex initial scalar field, a)-d) - plot viewing angle ($90^\circ, 0^\circ$), $t = T/2$: a) ICON FFSL, limiter [32], [23] b) standart adjoint c) art. source adjoint, limiter [32], [23] d) art. source adjoint, limiter [32], [6]

Table 4 Solid body rotation, cosine bell, grid R2B04, $T = 1036800[s]$

Error norms	ICON-FFSL, no limiter	Standard adjoint, no limiter	Art. source adjoint, no limiter	ICON-FFSL, limiter [32], [23]	Art. source adjoint, limiter [32], [23]	ICON-FFSL, limiter [32], [6]	Art. source adjoint, limiter [32], [6]
$l_{1,rel}$	2.230227E-02	4.617754E-02	2.230230E-02	1.399967E-02	1.399982E-02	1.358807E-02	1.358786E-02
$l_{2,rel}$	1.264162E-02	2.890380E-02	1.264118E-02	1.073500E-02	1.073535E-02	1.297653E-02	1.297682E-02
$l_{3c,rel}$	1.145005E-02	2.296593E-02	1.145946E-02	1.516152E-02	1.516201E-02	2.414110E-02	2.414264E-02
$l_{1,abs}$	3.737112	7.697128	3.737118	2.330792	2.330815	2.247145	2.247110
$l_{2,abs}$	1.245850E-01	2.838235E-01	1.245807E-01	1.055754E-01	1.055789E-01	1.269004E-01	1.269035E-01
$l_{3c,abs}$	1.134216E-02	2.273165E-02	1.134256E-02	1.500686E-02	1.500734E-02	2.389484E-02	2.389635E-02
Undershoot	9993	10007	9993	0	0	0	89
Minimum	-1.081394E-02	-1.164300E-02	-1.081451E-02	0	0	0	-5.023336E-11
Overshoot	0	2	0	4	4	4	4
Maximum	9.897216E-01	9.952338E-01	9.897270E-01	9.909216E-01	9.909271E-01	9.905530E-01	9.905582E-01

Table 5 Solid body rotation, slotted cylinder, grid R2B04, $T = 1036800[s]$

Error norms	ICON-FFSL, no limiter	Standard adjoint, no limiter	Art. source adjoint, no limiter	ICON-FFSL, limiter [32], [23]	Art. source adjoint, limiter [32], [23]	ICON-FFSL, limiter [32], [6]	Art. source adjoint, limiter [32], [6]
$l_{1,rel}$	3.069264E-01	3.171004E-01	3.069262E-01	2.522601E-01	2.522586E-01	2.599566E-01	2.599549E-01
$l_{2,rel}$	2.673495E-01	2.693426E-01	2.673488E-01	2.676666E-01	2.676659E-01	2.736425E-01	2.736418E-01
$l_{3c,rel}$	7.106978E-01	6.999076E-01	7.107034E-01	8.149918E-01	8.150041E-01	8.057034E-01	8.057114E-01
$l_{1,abs}$	3.157555E+02	3.263074E+02	3.157552E+02	2.593519E+02	2.593502E+02	2.669324E+02	2.669305E+02
$l_{2,abs}$	8.582671	8.649268	8.582646	8.586382	8.586358	8.773138	8.773115
$l_{3c,abs}$	7.106978E-01	6.999076E-01	7.107034E-01	8.149918E-01	8.150041E-01	8.057034E-01	8.057114E-01
Undershoot	9666	9649	9666	0	0	0	117
Minimum	-2.736402E-01	-2.657430E-01	-2.736436E-01	0	0	0	-8.511675E-10
Overshoot	435	431	435	415	415	414	414
Maximum	1.2450956	1.246481	1.245110	1.284667	1.284693	1.327834	1.327850

Table 6 Deformational flow, cosine bells, non-divergent velocity vector, grid R2B04, $T = 1036800[s]$

Error norms	ICON-FFSL, no limiter	Standard adjoint, no limiter	Art. source adjoint, no limiter	ICON-FFSL, limiter [32], [23]	Art. source adjoint, limiter [32], [23]	ICON-FFSL, limiter [32], [6]	Art. source adjoint, limiter [32], [6]
$l_{1,rel}$	3.256092E-02	4.011542E-02	3.256965E-02	2.342655E-02	2.341489E-02	1.895446E-02	1.894835E-02
$l_{2,rel}$	2.464795E-02	2.847823E-02	2.463155E-02	2.138599E-02	2.136528E-02	1.901537E-02	1.899423E-02
$l_{3c,rel}$	3.967162E-02	4.035984E-02	3.958678E-02	3.179198E-02	3.170231E-02	2.966709E-02	2.957616E-02
$l_{1,abs}$	2.438983E+01	2.999117E+01	2.439604E+01	1.759734E+01	1.758865E+01	1.427368E+01	1.426911E+01
$l_{2,abs}$	5.131036E-01	5.930658E-01	5.127594E-01	4.469183E-01	4.464925E-01	3.979740E-01	3.975392E-01
$l_{3c,abs}$	3.969944E-02	4.035763E-01	3.958461E-02	3.179024E-02	3.170058E-02	2.966546E-02	2.957454E-02
Undershoot	9201	9209	9208	0	0	0	1167
Minimum	-2.355757E-02	-2.397034E-02	-2.360643E-02	0	0	0	-8.922257E-10
Overshoot	0	1	0	0	0	0	0
Maximum	9.995831E-01	1.004633	9.994996E-01	9.988715E-01	9.987885E-01	9.991847E-01	9.991020E-01

Table 7 Deformational flow, slotted cylinders, non-divergent velocity vector, grid R2B04, $T = 1036800[s]$

Error norms	ICON-FFSL, no limiter	Standard adjoint, no limiter	Art. source adjoint, no limiter	ICON-FFSL, limiter [32], [23]	Art. source adjoint, limiter [32], [23]	ICON-FFSL, limiter [32], [6]	Art. source adjoint, limiter [32], [6]
$l_{1,rel}$	2.890181E-01	2.888711E-01	2.889820E-01	2.780968E-01	2.780884E-01	2.738582E-01	2.738496E-01
$l_{2,rel}$	2.940940E-01	2.942568E-01	2.940659E-01	3.042498E-01	3.042283E-01	3.015322E-01	3.015094E-01
$l_{3c,rel}$	9.425960E-01	9.190518E-01	9.412042E-01	9.509492E-01	9.504477E-01	9.468321E-01	9.464949E-01
$l_{1,abs}$	6.834999E+02	6.832123E+02	6.834093E+02	6.576075E+02	6.575934E+02	6.475465E+02	6.475301E+02
$l_{2,abs}$	1.430822E+01	1.431595E+01	1.430670E+01	1.480470E+01	1.480354E+01	1.467501E+01	1.467376E+01
$l_{3c,abs}$	9.425960E-01	9.190518E-01	9.412042E-01	9.509492E-01	9.504477E-01	9.468321E-01	9.464949E-01
Undershoot	8886	8879	8890	0	0	0	181
Minimum	-9.581544E-02	-1.741285E-01	-9.600165E-02	0	0	0	-1.739492E-09
Overshoot	910	910	909	796	796	837	837
Maximum	1.193710	1.202044	1.193843	1.169024	1.169178	1.183066	1.183258

6.2.2. Tables for advection tests.

Table 8 Deformational flow, cosine bells, divergent velocity vector, grid R2B04, $T = 1036800[s]$

Error norms	Standard adjoint, no limiter	Art. source adjoint, no limiter	Art. source adjoint, limiter [32], [23]	Art. source adjoint, limiter [32], [6]
$l_{1,rel}$	4.029138E-002	3.311189E-002	1.753717E-002	1.627544E-002
$l_{2,rel}$	3.351494E-002	2.831085E-002	1.925266E-002	1.848417E-002
$l_{\infty,rel}$	5.717197E-002	4.793155E-002	3.574307E-002	3.388867
$l_{1,abs}$	3.013273E+001	2.479282E+001	1.305616E+001	1.210955E+001
$l_{2,abs}$	6.964130E-001	5.885914E-001	3.994988E-001	3.835561E-001
$l_{\infty,abs}$	5.710458E-002	4.787505E-002	3.570094E-002	3.384873E-001
Undershoot	9187	9189	0	7135
Minimum	-3.020335E-002	-2.661911E-002	0	-1.572671E-008
Overshoot	0	0	0	0
Maximum	9.955241E-001	9.937946E-001	9.933643E-001	9.933694E-001

Table 9 Deformational flow, slotted cylinders, divergent velocity vector, grid R2B04, $T = 1036800[s]$

Error norms	Standard adjoint, no limiter	Art. source adjoint, no limiter	Art. source adjoint, limiter [32], [23]	Art. source adjoint, limiter [32], [6]
$l_{1,rel}$	3.201877E-001	3.072660E-01	2.959957E-01	2.911967E-01
$l_{2,rel}$	3.004045E-001	2.950234E-01	3.033951E-01	3.008232E-01
$l_{\infty,rel}$	8.202367E-001	8.689133E-01	8.527525E-01	8.511831E-01
$l_{1,abs}$	6.792025E+002	6.511061E+02	6.267315E+02	6.163679E+02
$l_{2,abs}$	1.383153E+001	1.357617E+01	1.396507E+01	1.384493E+01
$l_{\infty,abs}$	8.202369E-001	8.689133E-01	8.527525E-01	8.511831E-01
Undershoot	8935	8867	14	7445
Minimum	-1.334238E-001	-1.173093E-01	-4.796964E-15	-4.019092E-09
Overshoot	858	839	791	801
Maximum	1.200032	1.185067	1.177634	1.179568

Table 10 Moving vortices, grid R2B04, $T = 1036800[s]$

Error norms	Standard adjoint, no limiter	Art. source adjoint, no limiter	Art. source adjoint, limiter [32], [23]	Art. source adjoint, limiter [32], [6]
$l_{1,rel}$	2.412546E-02	1.411150E-03	1.411459E-03	1.411150E-03
$l_{2,rel}$	4.083858E-02	3.874989E-03	3.875515E-03	3.874989E-03
$l_{\infty,rel}$	2.048717E-01	3.017727E-02	3.017801E-02	3.017727E-02
$l_{1,abs}$	5.084637E+02	2.881504E+01	2.882144E+01	2.881504E+01
$l_{2,abs}$	6.294867	5.789490	5.790304	5.789490E-01
$l_{\infty,abs}$	3.148948E-01	4.638326E-02	4.638440E-02	4.638326E-02
Undershoot	44	1	1	1
Minimum	4.483181E-01	4.629725E-01	4.629725E-01	4.629725E-01
Overshoot	259	1	1	1
Maximum	1.613474	1.537027	1.537027	1.537027

6.3. Numerical results of data assimilation tests.

6.3.1. Figures for data assimilation tests.

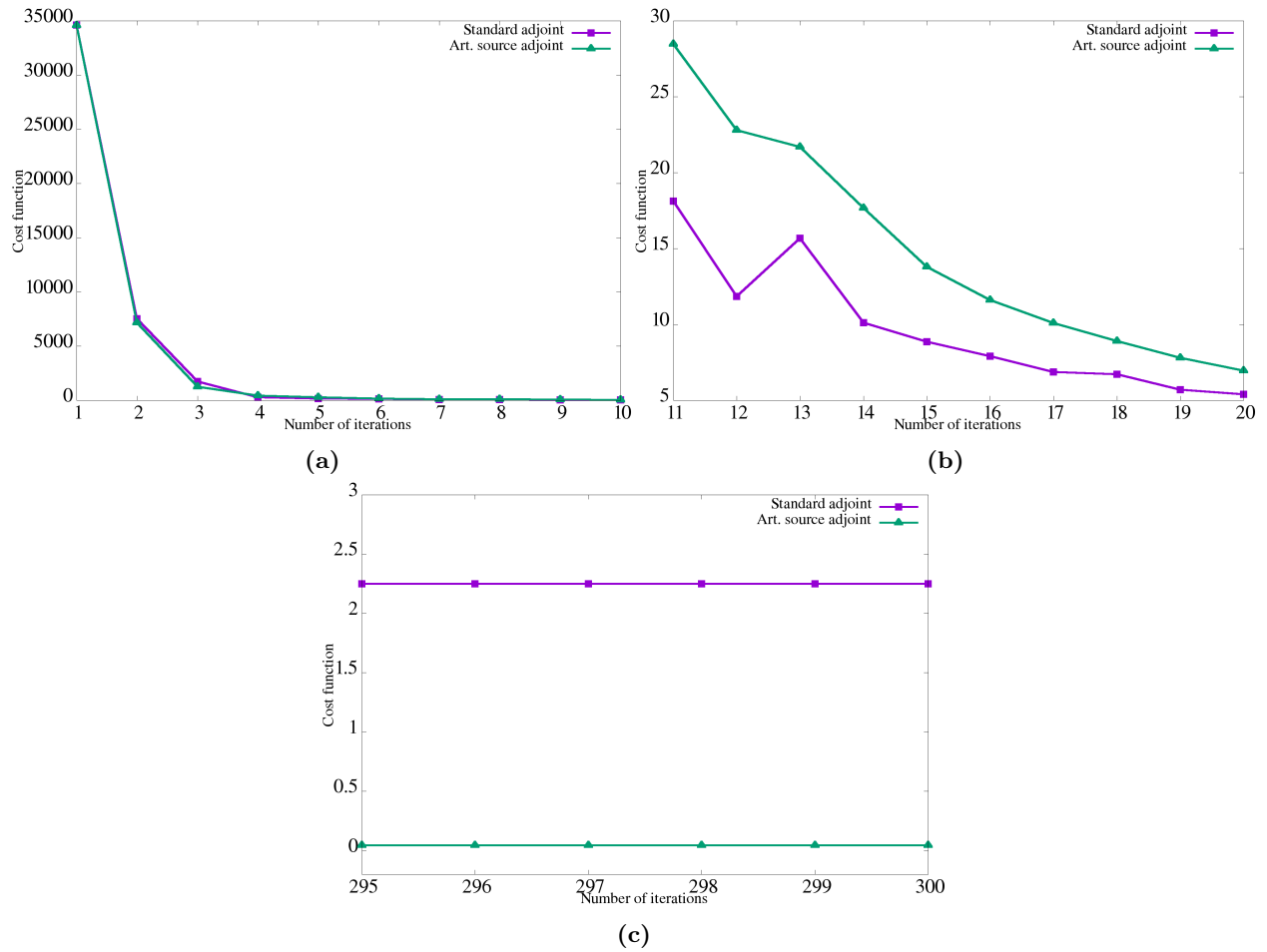


Fig. 16 Effect of number of iterations, deformational flow with cosine bells, $R2B4$ grid, 5120 observation points, number of iterations on abscissa, cost function on ordinate a) iterations from 1 to 10 b) iterations from 11 to 20 c) iterations from 295 to 300

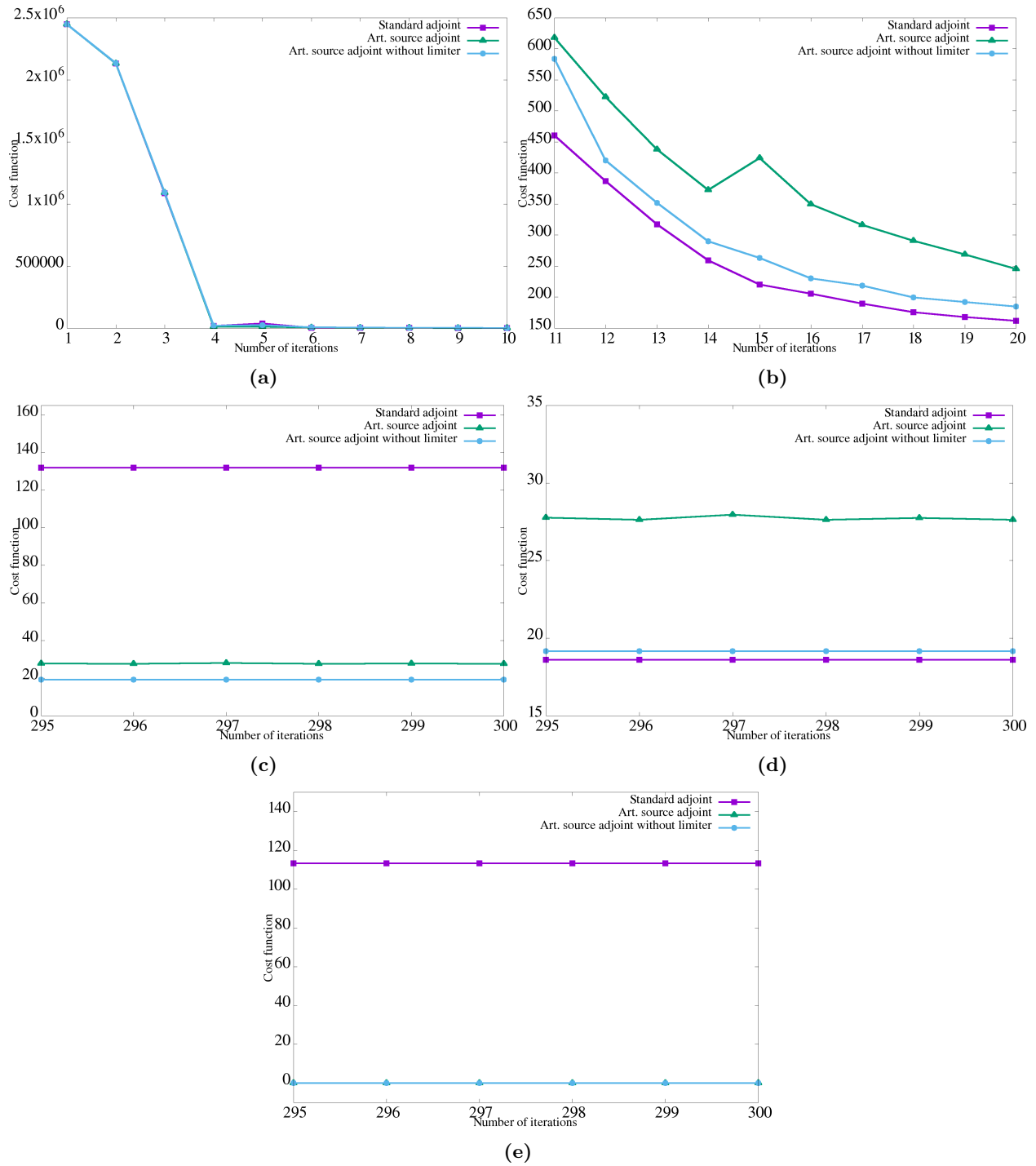


Fig. 17 Effect of number of iterations, moving vortex, *R2B4* grid, 5120 observation points, number of iterations on abscissa, cost function on ordinate a) iterations from 1 to 10 b) iterations from 11 to 20 c) iterations from 295 to 300 d) background term only, iterations from 295 to 300 e) observation term only, iterations from 295 to 300

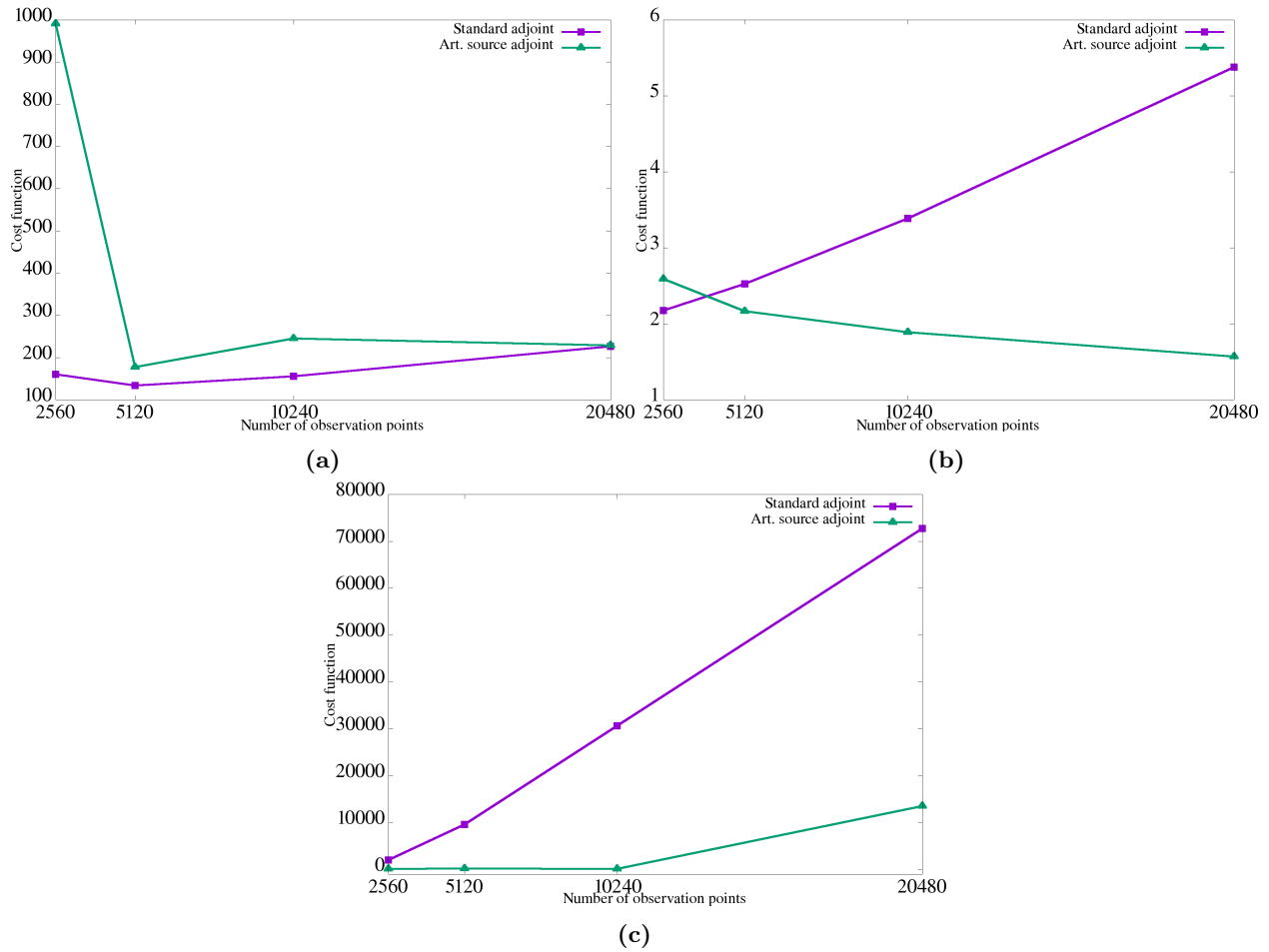


Fig. 18 Effect of observations, $R2B4$ grid, number of observation points on abscissa, cost function on ordinate a) moving vortex b) deformational flow, cosine bells c) deformational flow, slotted cylinders

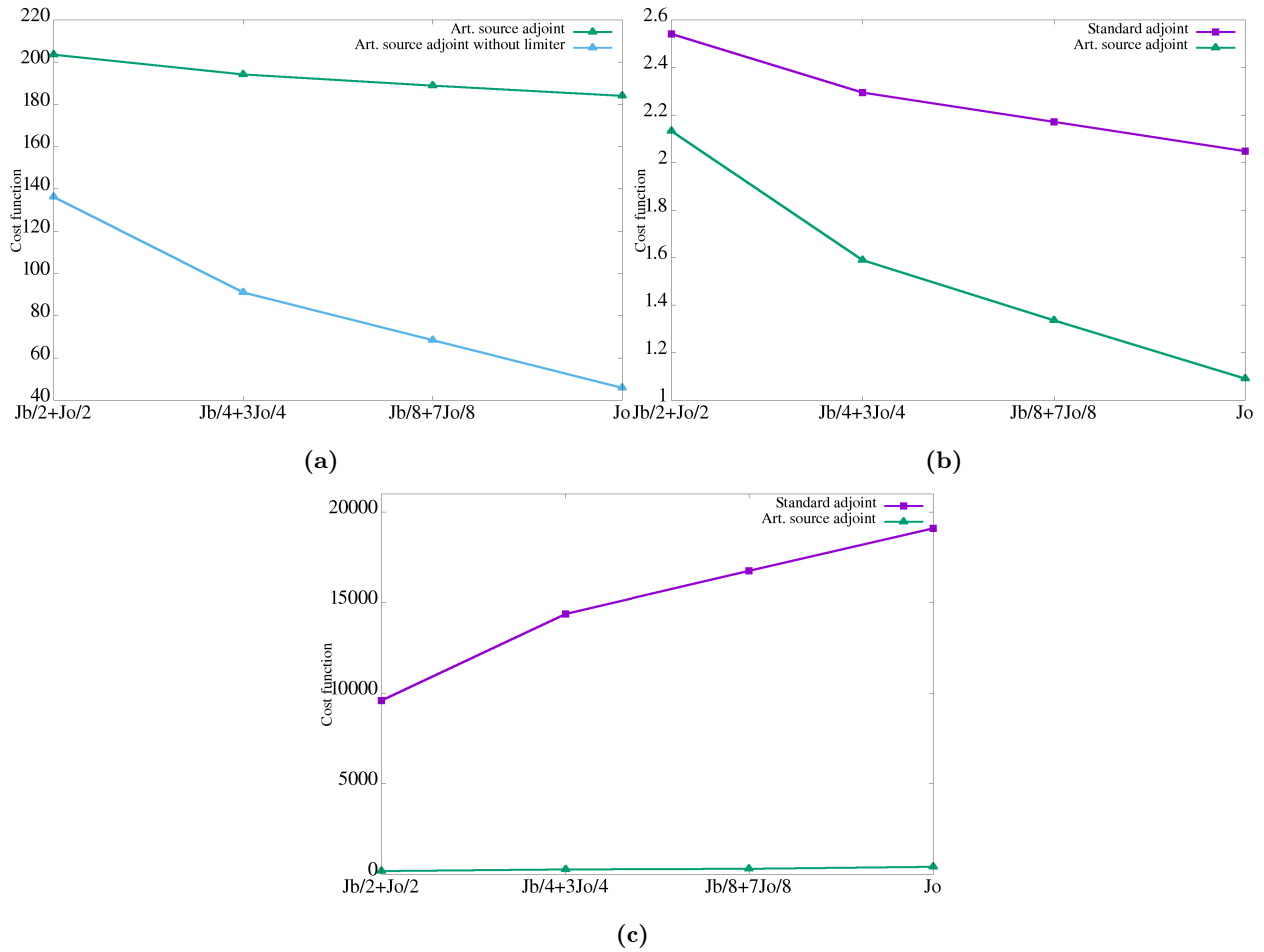


Fig. 19 Effect of weights of background and observation terms, $R2B4$ grid, 5120 observation points, cost function with different weights for background and observation term on abscissa, value of cost function on ordinate a) moving vortex b) deformational flow, cosine bells c) deformational flow, slotted cylinders

Table 11 Error in initial scalar field before and after assimilation. Cost function $J = J_o$, grid $R2B04$, 5120 observation points, 50 iterations

v	q_0	Error norms	Initial error	Standard adjoint	Art. source adjoint
3	4	$l_{1,rel}$	1.69E-01	1.79E-02	1.93E-02
		$l_{2,rel}$	8.39E-02	1.45E-02	1.94E-02
		$l_{\infty,rel}$	1.0E-01	1.64E-02	5.45E-02
		$l_{1,abs}$	1.27E+02	1.36E+01	1.48E+01
		$l_{2,abs}$	1.75	3.06E-01	4.14E-01
		$l_{\infty,abs}$	1.0E-01	1.64E-02	5.45E-02
3	5	$l_{1,rel}$	9.32E-02	1.42E-01	1.86E-02
		$l_{2,rel}$	7.37E-02	1.58E-01	2.0E-02
		$l_{\infty,rel}$	1.0E-01	8.7E-01	1.38E-01
		$l_{1,abs}$	1.98E+02	3.02E+02	3.98E+01
		$l_{2,abs}$	3.39	7.3	9.22E-01
		$l_{\infty,abs}$	1.0E-01	8.7E-01	1.38E-01
v	q_0	Error norms	Initial error	Art. source adjoint without limiter	Art. source adjoint
4	3	$l_{1,rel}$	1.0E-01	1.09E-03	2.4E-03
		$l_{2,rel}$	1.0E-01	3.55E-03	4.4E-03
		$l_{\infty,rel}$	1.0E-01	1.0E-01	1.99E-01
		$l_{1,abs}$	2.05E+03	2.31E+01	4.98E+01
		$l_{2,abs}$	1.5E+01	5.79E-01	7.0E-01
		$l_{\infty,abs}$	1.54E-01	1.54E-01	3.06E-01

6.3.2. Tables for data assimilation tests.

Table 12 Effect of mesh refinement on cost function, 20480 observation points, 50 iterations

v	q_0	Grid	Cost	Art. source adjoint without limiter	Art. source adjoint with limiter		
3	4	<i>R2B4</i>	Initial	1.38305576E+05	1.382259723E+05		
			Final	5.43400710	1.568333807		
		<i>R2B5</i>	Initial	1.38485396E+05	1.384239895E+05		
			Final	7.25133893	7.422831065		
		<i>R2B6</i>	Initial	1.38514151E+05	1.384673924E+05		
			Final	6.07498723E+04	6.838604955E+01 ¹		
		<i>R2B7</i>	Initial	1.38572302E+05	1.384887423E+05		
			Final	1.38570810E+05 ¹	2.653808533E+02		
		3	5	<i>R2B4</i>	Initial	9.28758721E+05	4.88312986E+05
					Final	7.42488109E+04	1.24677839E+02
<i>R2B5</i>	Initial			7.74514390E+05	4.98244461E+05		
	Final			2.89551111E+04	2.49163938E+02		
<i>R2B6</i>	Initial			7.22016145E+05	5.02445988E+05		
	Final			4.64099399E+05	6.98240016E+02		
<i>R2B7</i>	Initial			1.44938992E+06	5061026074E+05		
	Final			1.12492223E+06	1.38281501E+03		
4	3			<i>R2B4</i>	Initial	9.79289433E+06	9.79289444E+06
					Final	2.26422983E+02	2.29100238E+02
		<i>R2B5</i>	Initial	9.79276206E+06	9.79276221E+06		
			Final	4.79062588E+02	2.42988014E+02		
		<i>R2B6</i>	Initial	9.79280057E+06	9.79280054E+06		
			Final	9.79280057E+06	3.04970940E+05		
		<i>R2B7</i>	Initial	—	—		
			Final	—	—		

¹ Iteration 51, as iteration 50 was the first iteration after restart, where $\alpha = 1$

6.4. Coefficients of adjoint scheme.

$$\begin{aligned}
\alpha_{j0} &= \sum_{e=1}^3 \gamma_e \beta_{j0}^e, & \alpha_{j1} &= \sum_{e=1}^3 \gamma_e \beta_{j1}^e, & \alpha_{j2} &= \sum_{e=1}^3 \gamma_e \beta_{j2}^e, & \alpha_{j3} &= \sum_{e=1}^3 \gamma_e \beta_{j3}^e, \\
\alpha_{j4} &= \gamma_1 \beta_{j4}^1 + \frac{1}{2}(1+s_2)\gamma_2 \beta_{j4}^2 + \frac{1}{2}(1+s_3)\gamma_3 \beta_{j4}^3, \\
\alpha_{j5} &= \gamma_1 \beta_{j5}^1 + \frac{1}{2}(1+s_2)\gamma_2 \beta_{j5}^2 + \frac{1}{2}(1+s_3)\gamma_3 \beta_{j5}^3, \\
\alpha_{j6} &= \gamma_2 \beta_{j6}^2 + \frac{1}{2}(1+s_1)\gamma_1 \beta_{j6}^1 + \frac{1}{2}(1+s_3)\gamma_3 \beta_{j6}^3, \\
\alpha_{j7} &= \gamma_2 \beta_{j7}^2 + \frac{1}{2}(1+s_1)\gamma_1 \beta_{j7}^1 + \frac{1}{2}(1+s_3)\gamma_3 \beta_{j7}^3, \\
\alpha_{j8} &= \gamma_3 \beta_{j8}^3 + \frac{1}{2}(1+s_1)\gamma_1 \beta_{j8}^1 + \frac{1}{2}(1+s_2)\gamma_2 \beta_{j8}^2, \\
\alpha_{j9} &= \gamma_3 \beta_{j9}^3 + \frac{1}{2}(1+s_1)\gamma_1 \beta_{j9}^1 + \frac{1}{2}(1+s_2)\gamma_2 \beta_{j9}^2, \\
\alpha_{j10} &= \frac{1}{2}(1-s_1)\gamma_1 \beta_{j10}^1, & \alpha_{j11} &= \frac{1}{2}(1-s_1)\gamma_1 \beta_{j11}^1, \\
\alpha_{j12} &= \frac{1}{2}(1-s_1)\gamma_1 \beta_{j12}^1 + \frac{1}{2}(1-s_2)\gamma_2 \beta_{j12}^2, \\
\alpha_{j13} &= \frac{1}{2}(1-s_2)\gamma_2 \beta_{j13}^2, & \alpha_{j14} &= \frac{1}{2}(1-s_2)\gamma_2 \beta_{j14}^2, \\
\alpha_{j15} &= \frac{1}{2}(1-s_2)\gamma_2 \beta_{j15}^2 + \frac{1}{2}(1-s_3)\gamma_3 \beta_{j15}^3, \\
\alpha_{j16} &= \frac{1}{2}(1-s_3)\gamma_3 \beta_{j16}^3, & \alpha_{j17} &= \frac{1}{2}(1-s_3)\gamma_3 \beta_{j17}^3, \\
\alpha_{j18} &= \frac{1}{2}(1-s_1)\gamma_1 \beta_{j18}^1 + \frac{1}{2}(1-s_3)\gamma_3 \beta_{j18}^3
\end{aligned}$$

where $\gamma_e = s_e d_e l_e \bar{v}_e$. s_e indicates the orientation of the edge on the grid and is defined by direction of the normal at the edge, d_e is the layer thickness at the edge, $d_e = \frac{\tilde{l}_{e,2}}{\tilde{l}_e} d_{c,1} + (1 - \frac{\tilde{l}_{e,2}}{\tilde{l}_e}) d_{c,2}$, where $d_{c,i}$, $i = 1, 2$ is the layer thickness at cell centers on both sides of the edge, \tilde{l}_e is the distance between those cell centers and $\tilde{l}_{e,2}$ is the distance between edge midpoint and cell center. Layer thickness at cell centers are computed in pressure coordinates, see [28]. $|\Omega_e|$ is the area of departure region at e^{th} edge, $e = 1, 2, 3$.

$$K_{j1} = \begin{cases} \{0, 1, 2, 3, 4, 5, 6, 7, 8, 9\}, & \text{if } \bar{v}_1 > 0, \\ \{1, 5, 0, 4, 11, 12, 2, 3, 18, 10\}, & \text{otherwise} \end{cases}$$

$$K_{j2} = \begin{cases} \{0, 1, 2, 3, 4, 5, 6, 7, 8, 9\}, & \text{if } \bar{v}_2 > 0, \\ \{2, 6, 7, 0, 12, 13, 14, 15, 3, 1\}, & \text{otherwise} \end{cases}$$

$$K_{j3} = \begin{cases} \{0, 1, 2, 3, 4, 5, 6, 7, 8, 9\}, & \text{if } \bar{v}_3 > 0, \\ \{3, 0, 8, 9, 1, 2, 15, 16, 17, 18\}, & \text{otherwise} \end{cases}$$

\vec{p}_e is tracer independent gauss quadrature vector:

$$\begin{aligned}
p_{e,1} &= \sum_{k=1}^4 \omega_{e,k} |J_{e,k}|, & p_{e,2} &= \sum_{k=1}^4 \omega_{e,k} |J_{e,k}| \lambda_{e,k}, & p_{e,3} &= \sum_{k=1}^4 \omega_{e,k} |J_{e,k}| \theta_{e,k}, \\
p_{e,4} &= \sum_{k=1}^4 \omega_{e,k} |J_{e,k}| \lambda_{e,k}^2, & p_{e,5} &= \sum_{k=1}^4 \omega_{e,k} |J_{e,k}| \theta_{e,k}^2, & p_{e,6} &= \sum_{k=1}^4 \omega_{e,k} |J_{e,k}| \lambda_{e,k} \theta_{e,k}, \\
p_{e,7} &= \sum_{k=1}^4 \omega_{e,k} |J_{e,k}| \lambda_{e,k}^3, & p_{e,8} &= \sum_{k=1}^4 \omega_{e,k} |J_{e,k}| \theta_{e,k}^3, & p_{e,9} &= \sum_{k=1}^4 \omega_{e,k} |J_{e,k}| \lambda_{e,k}^2 \theta_{e,k}, \\
p_{e,10} &= \sum_{k=1}^4 \omega_{e,k} |J_{e,k}| \lambda_{e,k} \theta_{e,k}^2.
\end{aligned}$$

$(\lambda_{e,i}, \theta_{e,i})$ is the gauss quadrature points, $w_{e,i}$ is the weight and $J_{e,i}$ is the Jacobian of transformation, $i = \overline{1, 4}$.

\vec{c}_e is tracer dependent vector of 10 unknown coefficients:

$$\begin{aligned}
c_{e,1} &= q_{j,e}, & c_{e,2} &= \frac{\partial q_{j,e}}{\partial \lambda}, & c_{e,3} &= \frac{\partial q_{j,e}}{\partial \theta}, & c_{e,4} &= \frac{1}{2} \frac{\partial^2 q_{j,e}}{\partial \lambda^2}, & c_{e,5} &= \frac{1}{2} \frac{\partial^2 q_{j,e}}{\partial \theta^2}, \\
&\dots
\end{aligned}$$

Those unknown coefficients are the solution of least-square problem [20].

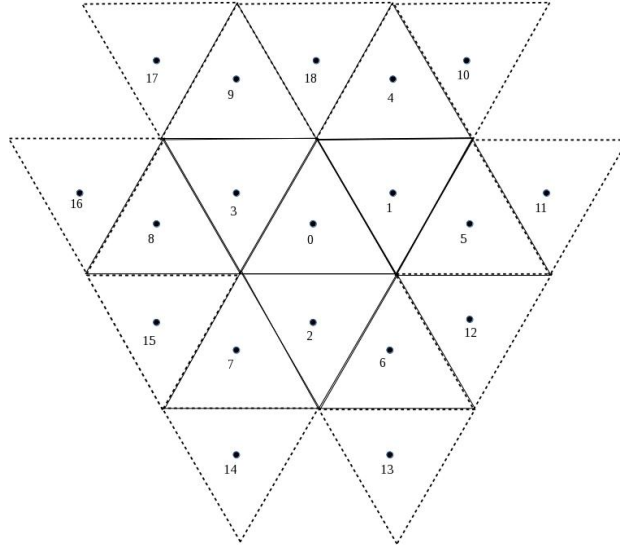


Fig. 20 Stencil on horizontal grid of ICON FFSL and its descendant adjoint scheme. Only bold triangles for ICON FFSL scheme stencil, bold and dashed triangles for adjoint scheme.

REFERENCES

- [1] H Elbern, J Schwinger, and R Botchorishvili, *Chemical state estimation for the middle atmosphere by four-dimensional variational data assimilation: System configuration*, Journal of Geophysical Research: Atmospheres **115** (2010), no. D6.

- [2] Hendrik Elbern and Hauke Schmidt, *A four-dimensional variational chemistry data assimilation scheme for eulerian chemistry transport modeling*, Journal of Geophysical Research: Atmospheres **104** (1999), no. D15, 18583–18598.
- [3] Hendrik Elbern, Hauke Schmidt, and Adolf Ebel, *Variational data assimilation for tropospheric chemistry modeling*, Journal of Geophysical Research: Atmospheres **102** (1997), no. D13, 15967–15985.
- [4] Tianyi Gou and Adrian Sandu, *Continuous versus discrete advection adjoints in chemical data assimilation with CMAQ*, Atmospheric environment **45** (2011), no. 28, 4868–4881.
- [5] P.E Haines, J.G Esler, and G.D Carver, *Adjoint formulation of the TOMCAT atmospheric transport scheme in the eulerian backtracking framework (retro-tom)*, Atmospheric Chemistry and Physics **14** (2014), no. 11, 5477–5493.
- [6] Lucas M Harris, Peter H Lauritzen, and Rashmi Mittal, *A flux-form version of the conservative semi-lagrangian multi-tracer transport scheme (cslam) on the cubed sphere grid*, Journal of Computational Physics **230** (2011), no. 4, 1215–1237.
- [7] Laurent Hascoet and Valérie Pascual, *The tapenade automatic differentiation tool: principles, model, and specification*, ACM Transactions on Mathematical Software (TOMS) **39** (2013), no. 3, 20.
- [8] Daven K Henze, Amir Hakami, and John H Seinfeld, *Development of the adjoint of geos-chem*, Atmospheric Chemistry and Physics **7** (2007), no. 9, 2413–2433.
- [9] Daniel Holdaway and James Kent, *Assessing the tangent linear behaviour of common tracer transport schemes and their use in a linearised atmospheric general circulation model*, Tellus A: Dynamic Meteorology and Oceanography **67** (2015), no. 1, 27895.
- [10] F Hourdin, O Talagrand, and A Idelkadi, *Eulerian backtracking of atmospheric tracers. ii: Numerical aspects*, Quarterly Journal of the Royal Meteorological Society **132** (2006), no. 615, 585–603.
- [11] PH Lauritzen, PA Ullrich, C Jablonowski, PA Bosler, D Calhoun, AJ Conley, T Enomoto, L Dong, S Dubey, and O Guba, *Geoscientific model development a standard test case suite for two-dimensional linear transport on the sphere: results from a collection of state-of-the-art schemes*, Geoscientific Model Development **7** (2014), no. 1, 105–145.
- [12] François-Xavier Le Dimet and Olivier Talagrand, *Variational algorithms for analysis and assimilation of meteorological observations: theoretical aspects*, Tellus A: Dynamic Meteorology and Oceanography **38** (1986), no. 2, 97–110.
- [13] Dong C. Liu and Jorge Nocedal, *On the limited memory bfgs method for large scale optimization*, Mathematical programming **45** (1989), no. 1-3, 503–528.
- [14] Zheng Liu and Adrian Sandu, *On the properties of discrete adjoints of numerical methods for the advection equation*, International journal for numerical methods in fluids **56** (2008), no. 7, 769–803.
- [15] Hiroaki Miura, *An upwind-biased conservative advection scheme for spherical hexagonal-pentagonal grids*, Monthly Weather Review **135** (2007), no. 12, 4038–4044.
- [16] Ramachandran D Nair and Christiane Jablonowski, *Moving vortices on the sphere: A test case for horizontal advection problems*, Monthly Weather Review **136** (2008), no. 2, 699–711.
- [17] Ramachandran D. Nair and Peter H. Lauritzen, *A class of deformational flow test cases for linear transport problems on the sphere*, Journal of Computational Physics **229** (2010), no. 23, 8868–8887.
- [18] Ramachandran D Nair and Bennert Machenhauer, *The mass-conservative cell-integrated semi-lagrangian advection scheme on the sphere*, Monthly Weather Review **130** (2002), no. 3, 649–667.
- [19] Maelle Nodet and Arthur Vidard, *Variational methods*, Handbook of Uncertainty Quantification (2016), 1–20.
- [20] Carl Ollivier-Gooch and Michael Van Altena, *A high-order-accurate unstructured mesh finite-volume scheme for the advection-diffusion equation*, Journal of Computational Physics **181** (2002), no. 2, 729–752.
- [21] Robert Sadourny, Akio Arakawa, and YALE Mintz, *Integration of the nondivergent barotropic vorticity equation with an icosahedral-hexagonal grid for the sphere*, Citeseer, 1968.
- [22] Adrian Sandu and Tianfeng Chai, *Chemical data assimilation An overview*, Atmosphere **2** (2011), no. 3, 426–463.
- [23] Christoph Schär and Piotr K Smolarkiewicz, *A synchronous and iterative flux-correction formalism for coupled transport equations*, Journal of Computational Physics **128** (1996), no. 1, 101–120.
- [24] Olivier Talagrand and Philippe Courtier, *Variational assimilation of meteorological observations with the adjoint vorticity equation. I: Theory*, Quarterly Journal of the Royal Meteorological Society **113** (1987), no. 478, 1311–1328.
- [25] John Thuburn and Thomas W.N Haine, *Adjoint of nonoscillatory advection schemes*, Journal of Computational Physics **171** (2001), no. 2, 616–631.
- [26] John Thuburn and Thomas WN Haine, *Nonoscillatory advection schemes with well-behaved adjoints*, Springer, 2001.
- [27] Tomislava Vukićević, Michele Steyskal, and Matthew Hecht, *Properties of advection algorithms in the context of variational data assimilation*, Monthly Weather Review **129** (2001), no. 5, 1221–1231.
- [28] Hui Wan, *Developing and testing a hydrostatic atmospheric dynamical core on triangular grids* (200901).
- [29] Hui Wan, Marco A Giorgetta, Günther Zängl, Marco Restelli, Detlev Majewski, Luca Bonaventura, Kristina Fröhlich, Daniel Reinert, P Ripodas, and Luis Kornblüeh, *The icon-1.2 hydrostatic atmospheric dynamical core on triangular grids, part i: formulation and performance of the baseline version*, Geoscientific Model Development **6** (2013), 735–763.
- [30] K-Y Wang, DJ Lary, DE Shallcross, SM Hall, and JA Pyle, *A review on the use of the adjoint method in four-dimensional atmospheric-chemistry data assimilation*, Quarterly Journal of the Royal Meteorological Society **127** (2001), no. 576, 2181–2204.

- [31] David L Williamson, John B Drake, James J Hack, Rüdiger Jakob, and Paul N Swarztrauber, *A standard test set for numerical approximations to the shallow water equations in spherical geometry*, Journal of Computational Physics **102** (1992), no. 1, 211–224.
- [32] Steven T Zalesak, *Fully multidimensional flux-corrected transport algorithms for fluids*, Journal of computational physics **31** (1979), no. 3, 335–362.